November 2020

Design and Implementation of Solid/Solid Phononic Crystal Structures in Lateral Extensional Thin-film Piezoelectric on Silicon Micromechanical Resonators

Abdulrahman Alsolami
University of South Florida

Follow this and additional works at: https://digitalcommons.usf.edu/etd

Part of the Electrical and Computer Engineering Commons

Design and Implementation of Solid/Solid Phononic Crystal Structures in Lateral Extensional

Thin-film Piezoelectric on Silicon Micromechanical Resonators

by

Abdulrahman Alsolami

A dissertation submitted in partial fulfillment
of the requirements for the degree of
Doctor of Philosophy
Department of Electrical Engineering
College of Engineering
University of South Florida

Major Professor: Jing Wang, Ph.D.
Sylvia Thomas, Ph.D.
Arash Takshi, Ph.D.
Rasim Guldiken, Ph.D.
Jiangfeng Zhou, Ph.D.

Date of Approval:
November 6, 2020

Keywords: Microelectromechanical Systems, Acoustics, Microfabrication, Quality Factor

Dedication

To my parents, my advisors, my friends

Table of Contents

List of Tables

List of Figures

Abstract

Achieving high quality factor in MEMS resonator devices is a critical demand for today's wireless communication and sensing technologies. In order to reach this goal, several dedicated prior works have been conducted based on published literature at different frequency ranges. Particularly, piezoelectrically transduced resonators, which are widely deployed in commercial wireless communication systems, could benefit from greatly improved qualify factor. So far, their development has evolved from thin film bulk acoustic resonators (FBAR's) using surface attached piezoelectric thin-film transducers with moderate Q factors to high Q resonators equipped with a side-supporting tether (anchor) attached vibrating resonators that allow the devices to operate at very high frequency (VHF) and ultra-high frequency (UHF) ranges.

This dissertation presents a newly developed fabrication methodology to replace existing expensive SOI technologies with much cheaper single crystalline wafers using a modified Single-Crystalline Reactive Etched and Metallization (SCREAM) process. Piezoelectrically transduced MEMS resonators have been fabricated at USF cleanroom facility, which have been designed and tested successfully in air with a quality factor of 1,528 and an insertion loss of -32.1 dB for a disk shaped resonators. A quality factor of 1,013 along with an insertion loss of -19 dB have been achieved for a rectangular plate resonator. In these devices, varied silicon layer thickness ranging from submicrons to tens of microns from a single layer were achieved as opposed to an uniform thickness of the device layer across the silicon-on-insulator (SOI) wafers, allowing device batch fabrication while maintaining the same number of photolithography steps. Resonators with varied

Si resonator structure layer thickness have been implemented and studied in terms of motional resistance (R_m), quality factor (Q) and resonance frequency.

To our best knowledge, this work has pioneered the implementation of soild/soild phononic crystals (PnCs) in fully suspended, lateral extensional and contour mode bulk acoustic wave (BAW) resonators. The in-house fabrication of the PnCs was performed on silicon-on-insulator (SOI) substrate. Silicon and tungsten were chosen as alternated layers for PnCs with a 4.5 ratio of acoustic impedance mismatch between the two chosen solid materials. The analysis of solid/solid PnCs bandgap is also conducted for determining the frequency regime, where no phonons exist. PnCs are strategically designed with piezoelectric transduction mechanism to operate within the phononic bandgap regime. Finite Element method (FEM) is also performed to investigate PnCs behavior in acoustic wave rejection, in which it was evaluated to be ~11 dB rejection per crystal.

Lastly, the fully released thin-piezo on silicon (TPoS) resonators in this work have been fabricated, characterized and modeled. The work of fabricating fully released BAW resonators with embedded PnCs one of the pioneering work of solid/solid PnCs in the MEMS resonator field. The electrical equivalent circuit parameters of the devices were extracted and the quality factors for these devices have shown 7-10 times enhancement as compared to counterparts without PnCs.

Chapter 1: Introduction

1.1 History of Periodic Structures

The study of periodic crystal structures have started since centuries ago in 1883 when the French mathematician, Gaston Floquet, introduced his theory in finding solutions to periodic differential equation. The Floquet's theory was then applied in solid-state physics by the American physicist Flex Bloch in 1928 which is known now as Bloch's theorem. These theories are applied to periodic structures in the electromagnetics and photonics field, known as photonic crystals (PtCs), or in mechanical field, whether elastic or acoustic, which is known as phononic crystals (PnCs).

The elastic wave study of the periodic structures have started since 1887 when Rayleigh investigated the effects of these periodic structures on the elastic waves. He pointed out that waves within a certain frequency ranges cannot propagate in the periodic structures. Then in early 1900s Leon Brillouin carry the study of the periodic structures to a further extend the level of understanding when he noticed that the waves' propagation through the periodic structures can be analyzed by studying one unit-cell structure only of the periodic structures in which he introduced the Brillouin zone of a single structure.

The idea of reflecting the sound waves utilizing periodic layers was first introduced by W. E. Newell in 1965 when he took the original ideas of Bragg reflector used in the optics/electromagnetic domain and applied them in the acoustic domain [1]. Newell work is known now as solid-mounted resonator (SMR) which is still used until now for enabling 4G and 5G

technologies in communication systems. These periodic layers in SMR is known now as one-dimensional phononic crystals (PnC).

In 1987, the work of E. Yablonovitch in PtCs have proven that these periodic structures have their unique frequency bands to reflect the electromagnetic waves by eliminating the photons emission [2]. Soon after that, the first published paper to show the comparison between the electronic and acoustic crystals (i.e. PtCs and PnCs) was introduced by M. S. Kushwaha in 1993[3]. Ever since Kushwaha's paper was published, the PnCs started to see its light largely in theoretical developments until 1995 when the first experimentally PnCs was introduced in Madrid by designing sculpture that attenuates the acoustic sound waves [4].

Further analysis were performed on Sempere's sculpture by M. S. Kushawaha in 1997, in which he proved computationally that the sculpture does not have a full band gap but instead the sound attenuation occurs because the PnCs density of state have a minimum dip at 1.67 kHz [5]. In 1998, the first experimentally PnCs was reported to possess bandgap in the frequency band of 1-1.120 MHz designed in aluminum alloy with holes filled with mercury [6]. Soon after that in the twentieth century, the investigation of PnCs has been widely explored globally and applied in different fields of physics and engineering.

One of the first unique works that has driven the interest towards PnCs is the localized resonant PnCs by Liu et al [7], where they proved that at a certain sonic frequency ranges, the PnCs exhibits negative acoustic property [7]. This discovery puts the PnCs in the same category as acoustic metamaterials, in which such artificial metamaterial's properties cannot be found in nature. In Liu et al paper, they showed the arrangement of macro-scale PnCs cubic shape operating under kHz [7].

Up until 2000, all the PnCs have been assembled manually and experimented in large scale dimensions in millimeters and centimeters, therefore resulting in a maximum operating frequency of 1 MHz. The larger the sizes of PnCs in lossy materials, the more difficult for them to be implemented in actual productions. Thus, these large scale handmade PnCs are not applicable in practical real-world devices. Miniaturizing PnCs from macro scale to micro and nano scales allowed them to operate in very-high frequencies (VHF) and ultra-high frequencies (UHF) while leveraging state-of-the-art microfabrication lab facilities, which allow them to be employed for the radio frequency (RF) device applications. In 2005, the first work of micro-scale PnCs has been demonstrated by Wu's group in slanted SAW devices [8]. Then, the work of micro-scale PnCs has been investigated and studied widely and intensively in both SAW and bulk acoustic wave devices (BAW) devices by several groups around the globe.

1.2 Literature Review

As mentioned above, the early designs of PnCs were often in macro scales, which in turn limits their operation at low frequencies. Researchers have spent a great deal of effort to develop the theoretical analysis approach of PnCs [9-16]. After miniaturizing PnC to micro-scale, the SAW and BAW devices integration with PnCs becomes feasible mainly for RF applications. Besides these RF device applications of PnCs, there are other PnC applications, which will be discussed later in the PnC applications section. In this section, a review of the literature of PnCs associated with microfabricated devices is discussed with a focus on SAW and BAW devices.

SAW devices were the first type of devices to incorporate PnCs in their designs for RF frequency ranges. One of the early works was demonstrated by L. Dhar and J. A. Rogers when they introduced the one dimensional PnCs that operated at 0.573 GHz [17]. Their PnCs with dimensions in micrometers was patterned on glass substrate [17].

Then the work of the two dimensional PnCs was first experimented in 2005 by T-T. Wu et al. when they observed the band gap effect of Si/air PnCs on the slanted interdigital fingers SAW [8]. Soon after that, several works were published on solid/air PnCs crystals using different varieties of solid materials such as SiC, AlN-TiN, LiNbO3, etc. to investigate the behaviors of the designs with PnCs [18-20].

The exploration of two dimensional PnCs was then continued to include solid/solid PnCs by R. H. Olsson and I. El-Kady, who lead a group of researchers at Sandia National Laboratories. Their works demonstrated several device studies using SiO_2/W PnC [21]. In their works, the materials were constructed to have high acoustic impedance material (e.g., W) filled in holes surrounded by the low acoustic impedance material (e.g., SiO_2). For signal transmission/detection, they implemented tapered couplers of aluminum nitride (AlN) transducers to study the behavior of PnCs.

Unlike the SAW devices where PnCs usage is built to control the acoustic wave, the PnCs usage in BAW devices is mainly limited to one purpose which is suppress the acoustic leakage from the devices. Intensive works of PnCs in BAW have been done during the years of PnCs exploration. In fact, one can argue that one of the main reasons that we reached todays' communication technology is the PnCs.

Solid-mounted resonator (SMR) devices, which are the commonly used in many cell phone filters and duplexers in the world and still will continue to be used in future technology, is in fact a special type of one dimensional PnC device. One dimensional PnCs, also known as acoustic Bragg reflectors, were first discovered in 1965 by W. E. Newell as we mentioned and was strictly applied in BAW devices operating in thickness mode[ref]. At that time, his idea was never considered as PnCs since the PnCs studies did not start untill decades later. Then, when the PnCs

was classified into three types, 1D, 2D and 3D PnCs, Newell's work, since it is 1D PnCs, has inspired the utilization of 2D PnCs to be applied in BAW devices operated in lateral extensional modes to achieve the same purpose as his work which is to reduce the acoustic leakage to obtain high quality factor (Q). The work in 1D PnCs was and still is of an utmost interest to lots of researches and companies especially since the 5G technology also needs SMR devices. It is worthwhile to mentioning that those who work in this type of research don't call it as 1D PnCs but instead naming it as acoustic Bragg reflectors. One of the latest works on 1D PnCs or acoustic Bragg reflectors in lateral BAW devices is done by R. H. Olsson et al. and W. Wang et al in their patents [22-23]. Olsson was the first who suggested that acoustic reflectors can be implemented in MEMS resonators in his patent. He showed the fabrication process methods to obtain suspended MEMS resonators with lateral acoustic reflectors [22]. W. Wang and D. Weinstein from Massachusetts Institution Technology (MIT) carried Olsson's work from a suspended MEMS resonator to apply it on unreleased MEMS resonator [23]. In their work, the unreleased MEMS resonator was integrated with CMOS transistor in one process to remove the need of the post processing of MEMS-CMOS integration [24]. In their paper, they showed one of their demonstrated devices which is a hybrid RF CMOS-MEMS resonator operates at 11.1 GHz at IBM's 32 nm transistor level using SOI process.

Other papers were also published by modifying the resonators anchors of in BAW resonators and reshaping the anchors to represent one repeated cells of PnCs in 1D towards the substrate. Unlike the works of Olsson and Wang where their PnCs are solid/solid, these PnCs are not constructed using two types of solid materials but instead just the device layer that is etched strategically in a certain shape to construct one PnCs cell, which is considered as solid/air PnCs

type. These BAW resonators were actuated capacitively and peizoelectrically and have shown improved Q factor with a 1.5 to 3 times of enhancement [25-27].

The building block of PnCs on these papers is in itself a unit cell which is a geometrically 2D PnCs but since it is repeated in one axes only, researchers categorize them as 1D PnCs [25-27]. Two dimensional PnCs in BAW devices have also been widely studied in publications. The main groups who investigated 2D solid/air PnCs in BAW devices are J. E.-Y. Lee's group from City University of Hong Kong and D. Weinstein group from MIT [28-29]. Weinstein's group applied 2D GaN/air PnCs on a released GaN resonator. Lee's work investigated incorporation of 2D PnCs by strategically etching holes around the thin-piezo on silicon (TPoS) resonators. In their work, the 2D PnCs was constructed using solid/air PnCs type and the Q enhancement due to the use of 2D PnCs has shown an improvement up to 4 times.

To the author's knowledge, the microfabrication of two dimensional solid/solid PnCs type in suspended lateral extensional mode BAW devices has been patent as an idea by R. H. Olsson but they have never been analyzed, fabricated or tested.

1.3 PnCs Applications

The development of high technology devices nowadays have not only improved people's quality of life but also have made it easier for us to be productive. Cell phones and computers, in particular, are the leading electronic devices used by everyone in the globe and such devices were enabled by manipulating and controlling the electrons in the semiconductor materials that led to the existence of these devices. Similarly, manipulating and controlling photons have also led to improve the electronic devices in the electromagnetic/optics devices which led to the existence of the fiber optics, electromagnetic waves and microwaves used in todays' wireless communications. By knowing the importance of the manipulation of electrons and photons in the electronics and

electromagnetics/optics waves, manipulating phonons in a similar fashion plays an important role in controlling sound waves. Controlling the sound waves has led to the devices in the acoustic and thermal fields. Much like their optics and electronic analogue, the control and manipulation of the sound waves is an essential solution that would solve lots of issues in different fields of applications that depend on the frequency spectrum. The operating frequencies of PnCs depends on their scales so in order to apply PnCs at higher frequencies, the PnCs miniaturization is a must. The dependency between the PnCs scale and its operation frequency regimes can be noticed clearly and as such the PnCs can be scaled accordingly to the frequency regime of interest of different applications [30-34].

Not only have Phononic crystals (PnCs) shown its effectiveness for acoustic isolation in SMR resonators [35], but also PnCs, in macro and micro scales, have been used in various applications such as signal processing and filtering [36, 37], acoustic sensing [38], thermal energy scavenging via thermoelectrics [39], energy harvesting [40], acoustic waveguides [9, 41, 42] and negative refractive devices [43, 44, 45]. Some of these innovative PnCs applications can be built and manipulated depending on the application interest [46-49].

The fact that these PnCs can be scaled using microfabrication technology to micro and nano scales to be able to work at very high frequency (VHF) band (up to 300 MHz) and ultra-high frequency (UHF) band (up to 3 GHz) have intrigued the interest in developing microfabricated PnCs devices [35]. Therefore, RF and wireless communication applications on these frequency bands can embrace and utilize the PnCs. The main applications for RF devices of PnCs include acoustic insulators, acoustic waveguides, cavities and filters.

One example of the employment of PnCs as acoustic insulators is the pioneering application of the PnCs in SMR devices. The ability to reflect the acoustic wave leakage from the

7

thin film resonators to the substrate using a stack of Bragg reflection mirrors have allowed them

to have higher Q factors and improved their power handling capability at the same time [50]. One

can argue that thin film resonators operating in thickness mode is the main enabler of today's RF

wireless communication demands. SMR have risen above all other types of resonators in today's

technology needs and was proven to operate at high frequencies up to 8 GHz, which makes them

the lead industry device types for duplexers [50]

MEMS lateral extensional mode resonators have shown its potential to replace RF switches

in RF front-end transceivers. Unlike the SMR resonators where the acoustic leakage happens

vertically along device thickness, the acoustic wave leakage in lateral extensional mode resonators

is occurring through the resonator side supporting anchors laterally. Hence, utilization of PnCs in

the anchors will not only result in increased Q factor, but also concurrently facilitate the

suppression of the spurious modes that appeared due to the mitigation of free boundaries [29].

The conventional waveguide mechanism in optics depends on the sum of the light

reflections by media of high and low medium indexes. This, in fact, has enabled PtCs, the

electromagnetics/optics analogue of PnCs, to be potentially suited and used in waveguide

applications. Therefore, similar to the optics analogue, the acoustic waveguide will potentially

utilize PnCs in this type of application. PnCs have shown its ability and effectiveness in controlling

the acoustic signals.

Acoustic waveguides can be implemented in different applications to gain several benefits

such as enabling slow sound to propagate through the delay line for communication applications,

collimation used in medical acoustic device applications and generally in acoustic imaging

applications used in today's technology in which the signals from the transmitters need to be

controlled until they get detected by the receivers [51-55]. Acoustic cavities and filters is arguably

one of the most promising application of PnCs in communication field. Not only micro PnCs will allow the cavities in high quality material to operate at RF frequencies but they also will enhance the RF devices performance, which can be seen as in key performance metrics improvement such as insertion loss reduction and better frequency selection [18]. PnCs cavities and filters are a problem solver to the tradeoff between the current two key technologies in MEMS resonators [56]. Energy storage in high-Q materials using PnCs can overcome the trade-off between the need of high Q and low motional resistance in the today's MEMS resonators technology [18].

Thermal application have also been utilizing PnCs to control the heat transfer using thermal phonons. Thermal phonon is essentially the same as the acoustic phonon by designing PnCs that manipulate and suppress thermal phonons in THz regimes [31]. These type of PnCs shows potential application in reducing thermal conductivity for high Q materials [57-59].

1.4 Motivation

Periodic structures are investigated widely by many groups around the globe. PnCs studies are not only a new and emerging topic in the past two decades but also they has covered everything that is needed to be covered. In fact, some types of PnCs in certain devices have not been experimentally demonstrated yet even though they were proposed by researchers who have studied their concepts via theoretical models. The majority of microfabricated devices in which PnCs was implemented are SAW and BAW devices. PnCs can be classified based on orientation geometry, including one, two and three dimensional, and the material types that construct them, such as solid and air materials. Three dimensional PnCs would indicate complexity in microfabrication technology, therefore 3D PnCs have not been a key interest for investigation. As discussed above, several group have investigated the effect of the PnCs in enhancing Q factors of BAW resonators or disrupting the SAW signals at frequencies of interest. This work plans to extend prior works in

PnCs investigation by introducing solid/solid PnCs in several lateral extensional BAW resonators. Different types of PnCs were introduced such as 1D and 2D dimensional PnCs and localized resonance structures. To the author's best knowledge, this work would be the first work of its kind in MEMS that utilize two dimensional solid/solid PnCs in suspended lateral extensional mode BAW devices.

1.5 Dissertation Organization

The dissertation is organized as follow: Chapter 1 is an introductory chapter to PnCs history, which also elaborate state of arts, applications and the motivations of this work. The fundamental description of periodic structures, PnCs theory and its bandgap analysis are explained in Chapter 2. In Chapter 3, the study of the development of MEMS BAW devices is illustrated (SCREAM paper will be included) then followed by PnCs fabrication in BAW resonators in chapter 4. Chapter 5 provides key concluding remarks and discussions followed by elaboration of the future works in Chapter 6.

1.6 Contribution

To the author's best knowledge, this work implements the solid/solid PnCs designs in suspended BAW devices for the first time. TPoS resonators using SOI wafers were incorporated with PnCs designs. The designs were fabricated in USF cleanroom at nanotechnology research education center (NREC). The design layout was drawn using CAD tool. The main designs of interest, 2D PnCs and 1D PnCs (Bragg reflectors), have been studied under different BAW resonator design implementations. The contributions of this work can be summarized as:

- Development of an optimized TPoS devices process using single crystalline silicon wafer by utilizing modified SCREAM process.

- Introducing the solid/solid PnCs for suspended MEMS BAW devices.

- Newly developed fabrication methods of solid/solid PnCs devices.

- Measuring and validating PnCs improvements on MEMS BAW devices behaviors, such as significant quality factor enhancement.

Chapter 2: Background

2.1 Periodic Structures

Nature has always been the curiosity factor and source of innovation for people that drives growing desire for technological evolution. Materials that are found in nature with their unique capabilities of manipulating heat, electricity and sound waves have drawn scientists' attentions while periodic structural designs done by animals, like spider webs and honeycombs, have fuel creativities of engineers. Certainly, people's curiosity have grown much bigger with increasing knowledge and technology evolution globally to meet the human daily life needs by studying and replicating the nature structures that are adopted by today's technology.

The man-made periodic structures, such as photonic crystals (PtCs) and phononic crystals (PnCs), hold unique abilities to reflect the light and the sound in the form of optical/electromagnetic and acoustic waves, respectively [3]. The created periodic structures generally are classified based on their axial periodicity as can be seen in Figure 2.1 that illustrates 1D, 2D and 3D PnCs structures.
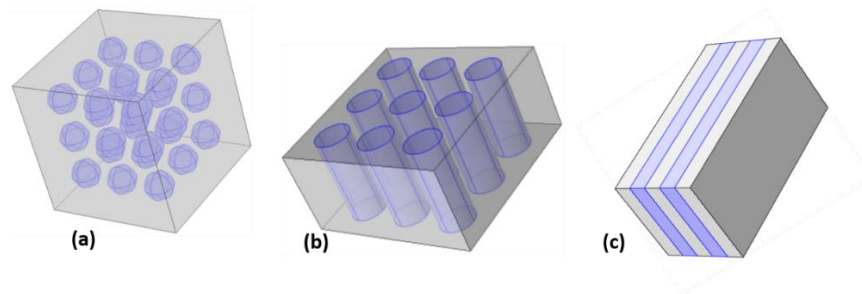
Figure 2.1 – Schematic illustration of phononic crystal (PnC) configuration of different dimensions or degree of freedoms, including (a) 3D PnCs; (b) 2D PnCs; (c) 1D PnCs.

The concept of PnCs, which is considered relatively new compared to other physics, has quickly progressed from just a topic of discussion among wave physics to be a key enabler for many device applications proposed by researchers. This topic has attracted a great deal of attention by researchers due to its applicability to many applications and its compatibility with CMOS or semiconductor IC batch fabrication.

This is indeed a hot topic for microstructure devices especially in MEMS field where acoustic wave manipulation is the core of this field. As mentioned earlier, many researchers have embedded PnCs in SAW devices to study their wave manipulation effects. The compatibility with MEMS fabrication allowed researchers to use PnCs with different substrates. Similar to photonic crystals, PnCs are periodic structures that are constructed while using different material properties. In photonic crystals, the dielectric constant (refractive index) is considered to be the most important material property, whereas in PnCs, the elastic properties (acoustic impedance and acoustic velocity) of the materials play an equally pivotal role.

PnCs are periodic structures that are constructed to control the acoustic wave propagation. Acoustic waves at certain frequencies are not allowed to propagate within or through the periodic structures due to the inability of phonons to pass in these regimes. These forbidden frequencies are often know as band gap. The band gap phenomena exist in engineered periodic structures such as photonic crystals for electromagnetic waves or phononic crystals for the acoustic waves. Similar to PtCs, the wavelengths range of these forbidden frequencies are in spatial order of the PnCs structure's key dimensions. The formation of the band gap occurs due to the scattering and reflections occurring to the incident waves, electromagnetic or acoustic/mechanical, inside the periodic structures. Depending on the geometrical dimension and material hosting of the PnCs, these waves are scattered differently.

This chapter will provide an overview of the theory of PnCs. The first section will be about the strategic choice of materials for construction of the PnCs. Then different geometrical dimensions of PnCs will be discussed in details. To reach the focal point of this research topic, more detailed theory will be included for modeling Bragg reflectors and two dimensional (2D) PnCs. Lastly, Brillouin-zone diagram will be introduced and discussed for clarifying the end goals of this research.

2.2 Mechanical Wave Propagation

Unlike photonic crystals (PtCs), phononic crystals (PnCs) cannot be constructed of the same material properties as PtCs, in which the dielectric property or refractive index is the defining factor of the PtCs. Instead, PnCs rely on the elastic properties of the material to influence and manipulate the propagation of acoustic waves. Unlike electromagnetic waves, which can travel through vacuum, the acoustic waves do not travel through vacuum due to its dependence upon the elasticity. The acoustic waves can travel in different ways in different medium. The transversal and longitudinal waves exist only in solid medium unlike the fluid medium where the transversal waves do not exist because the shear deformation does not exist in fluid materials [61,62].

The acoustic waves can be understood by the movements of the atoms inside the crystal material. If the atoms move along the direction of the wave then the waves are referred to as longitudinal wave, whereas if they moved perpendicular to the wave then the waves are called transversal waves. Figure 2.2 shows the ordinary state of atoms in the crystalline material and how these atoms are disrupted when the incident mechanical waves come in and propagate through them[0,2].

The governing equation of the mechanical wave propagating through a materials is given by [62]:

$$\nabla^2 u = \frac{1}{c^2} \frac{\partial^2 u}{\partial t^2} \tag{2.1}$$

where u stands for the displacement and c stands for the phase acoustic velocity
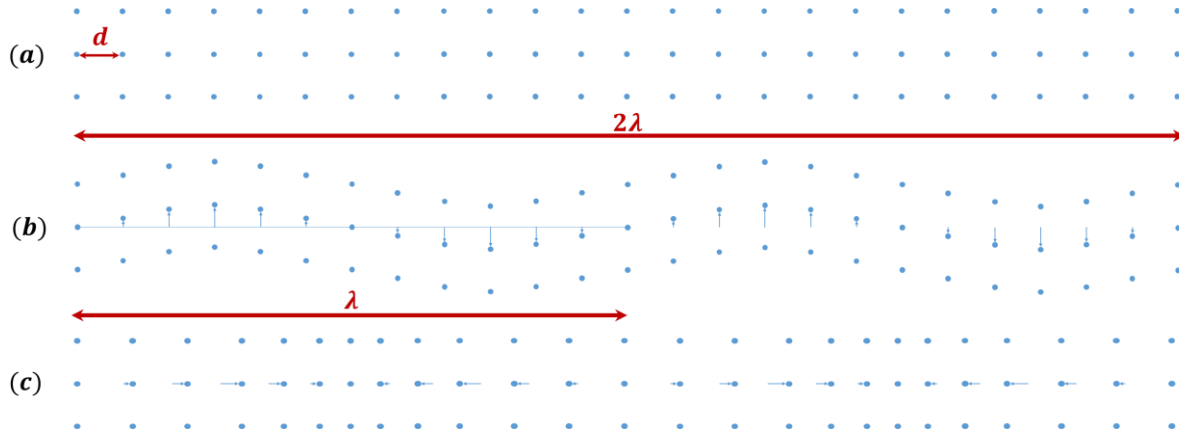
Figure 2.2 – Illustration of elastic material atoms distribution by mechanical wave, including (a) atoms distribution in a (normal) steady state; (b) Atoms displacement due to the transverse wave propagate within the material; (c) atoms displacement due to the longitudinal wave propagate within the material.

The formula of the mechanical plane waves at a specific frequency are given by [62]:

$$u(r,t) = Re(u_0 e^{i(k.r-\omega t)}) \tag{2.2}$$

where r represents the location, the relationship between the k vector and the frequency can be solved using the equations (2.1) and (2.2) [62]:

$$k = |\boldsymbol{k}| = \frac{\omega}{c} \tag{2.3}$$

The velocity of the mechanical plane wave depends on the material properties and different formulas can be used for different mechanical waves as follow [62]:

$$c^2 = \rho^{-1} * \begin{cases} \mu & \text{Transversal elastic wave} \quad (2.4) \\ (\lambda + 2\mu) & \text{Longitudinal elastic wave} \quad (2.5) \\ \lambda & \text{Longitudinal acoustic wave} \quad (2.6) \end{cases}$$

where, ρ is the density and μ and λ are the Lame's coefficients which are material property dependent that can be calculated as follow [62]:

15

$$\lambda = \frac{E\nu}{1 - \nu - 2\nu^2} \tag{2.7}$$

$$\mu = \frac{E}{2 + 2\nu} \tag{2.8}$$

where, E is the young modulus and ν is the Poisson's ratio.

Understanding how the wave propagate in the different material is important for PnCs analysis. PnCs can be constructed using solid-solid, fluid-fluid or solid-fluid structures. Each of above three cases is analyzed differently since the actual wave propagation mechanism is different in each type of material. Solid-solid PnCs have all the mechanical waves propagating through the structures unlike fluid-fluid PnCs where the transversal waves do not exist in the fluid material. On the other hand, Solid-fluid PnCs have more difficult operation mechanism or scenario. In solid-fluid PnCs, all mechanical waves propagate in the solid material in the PnC structure but only longitudinal waves propagate in the fluid structure. Not only do the type of the material affect the wave propagation, but also the shape of the PnCs have experimentally proven to have a great effect as evidenced by some strategically designed MEMS devices. Researchers have proven that PnCs can be employed to suppress the acoustic losses in MEMS resonators thus enhancing the quality factor. To compare between 2D PnCs and the acoustic Bragg reflector (known as 1D PnCs), the latter have proven to enhance the Q factor by almost 9 times as compared to the best achievable in unreleased MEMS resonator with 2D PnCs [44]. The next sections will discuss the strategic design of the dimensions of PnCs followed by the construction of the desired band gap in the Brillouin zone section.

2.3 Acoustic Bragg Reflector

The acoustic Bragg reflector (ABR), which is also known as 1D PnCs, is constructed using two different slab materials as depicted in the Figure 2.3. The reason ABR is sometimes used in

different terminology than PnCs is largely due to its existence since 1960s when W. E. Newell introduced this terminology of ABR [1]. Unlike ABR, the PnCs has seen its light to micro-scale devices ever since 2000s. Even though the PnCs development is of great interest to many researchers around the globe, ABR is still the dominant application in communication, specifically in making oscillators using piezoelectric based devices that meets today technology specifications.

To examine the ABR, the propagation of the mechanical waves at the interference between two different elastic materials with mismatched properties needs to be analyzed. By referring to Equations (4), (5) and (6), the propagation of elastic waves in materials can be explained by the materials properties such as the density, the wave velocity, the materials' Lame's coefficients, Young's modulus and Poisson's ratio (i.e., $\rho, c, \lambda, \mu, E, v$) as shown in Figure 2.3.
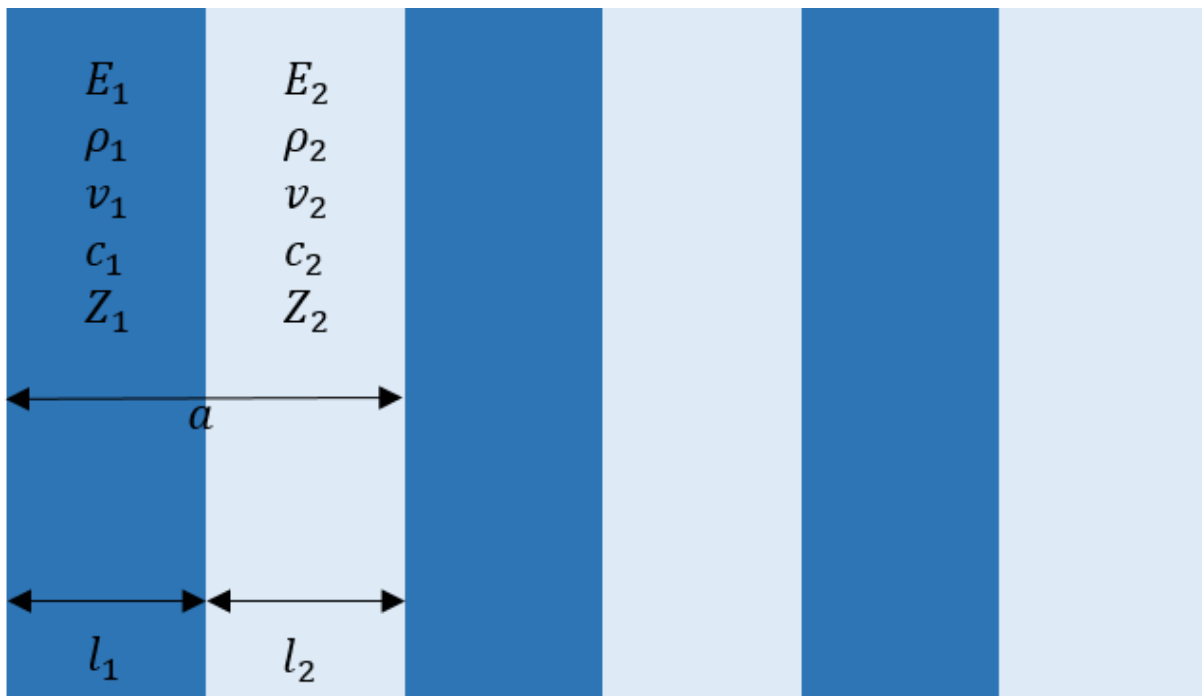
Figure 2.3 – Alternated materials 1 (blue) and material 2 (grey), which hold different elastic properties including Young's modulus, density, Poisson's ratio (E, ρ, v), and Z represents material's acoustic impedance, while c represents the phase velocity of mechanical waves in either longitudinal or transversal directions.

The acoustic impedance of the material can be evaluated by the following formula [56]:

$$Z_i = \sqrt{E_i \rho_i} \qquad (2.9)$$

In the ABR, the reflection of the incident waves occurs at the material interference between two dissimilar materials when there is an acoustic impedance mismatch as can be seen in Figure 2.4. Such technique was also implemented in capacitively transduced MEMS disk resonators to suppress the acoustic energy dissipation through center supporting anchor to the substrate by constructing a disk resonator in diamond while using silicon to form the center stem anchor [64].
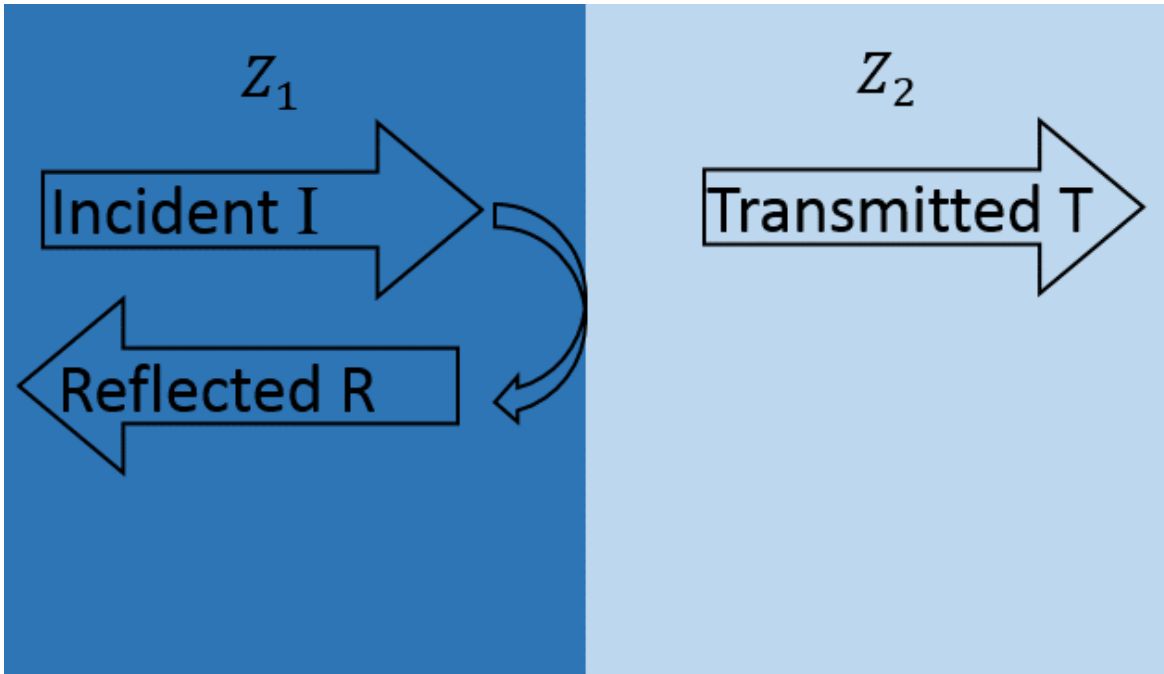
Figure 2.4 – The wave transmission and reflection that occurs at the interface between two different materials with dissimilar elastic/acoustic properties.

When a mechanical acoustic waves is transmitted, a portion of the energy is transmitted while the rest is reflected. The reflectivity and transmissivity through the interface of the two dissimilar materials can be calculated using the following equation [63]:

$$R = (Z_1 - Z_2) * (Z_1 + Z_2)^{-1} \qquad (2.10)$$

$$T = 1 - R \qquad (2.12)$$

18

The values of reflectivity and transmissivity changes according to the incident wave direction. The material pairs should be chosen carefully to induce a high reflection to improve devices performance by constructing one material to have much higher acoustic impedance compared to that of the other material. The ABR has proven its performance in unreleased MEMS resonator devices for implementation within transistor foundry process technology while remaining its high Q factor [24]. Similar to solid mounted resonators (SMRs), dimensions of quarter wavelength in length or thickness should be constructed to achieve the maximum reflectivity.

2.4 2D PnCs

The 2D PnCs are the most common PnCs used in devices and other applications. 2D PnCs allow the ability to strategically design the geometry that is not possible in the ABR while demanding less fabrication complexity as compared to 3D PnCs. Most of prior works on PnCs in contour mode MEMS resonators, especially in the field of microfabricated PnCs, are in the category of 2D PnCs for these reasons. As seen in Figure 2.1, 2D PnCs is constructed by manipulating the geometry in two key dimensions (typically the in-plane dimensions), while the third is assumed to be infinite. As mentioned earlier, PnCs exist in three forms, which are fluid-fluid, solid-solid, or solid-fluid PnCs. Since it is almost unrealistic to fabricate fluid-fluid PnCs in micro-scale devices, especially MEMS devices, this type of PnCs will be not be the focus in this research. Solid-solid and fluid-solid PnCs are not only commonly used in micro-scale devices but also very realistic for evaluating the mechanical waves, since both types of PnCs support all kinds of mechanical waves. To examine the wave propagation in 2D PnCs using numerical analysis, it is very important to plot the band diagram of PnCs based on the repetition of structures. Figure 2.5 shows the direct lattices of 2D periodic structures.
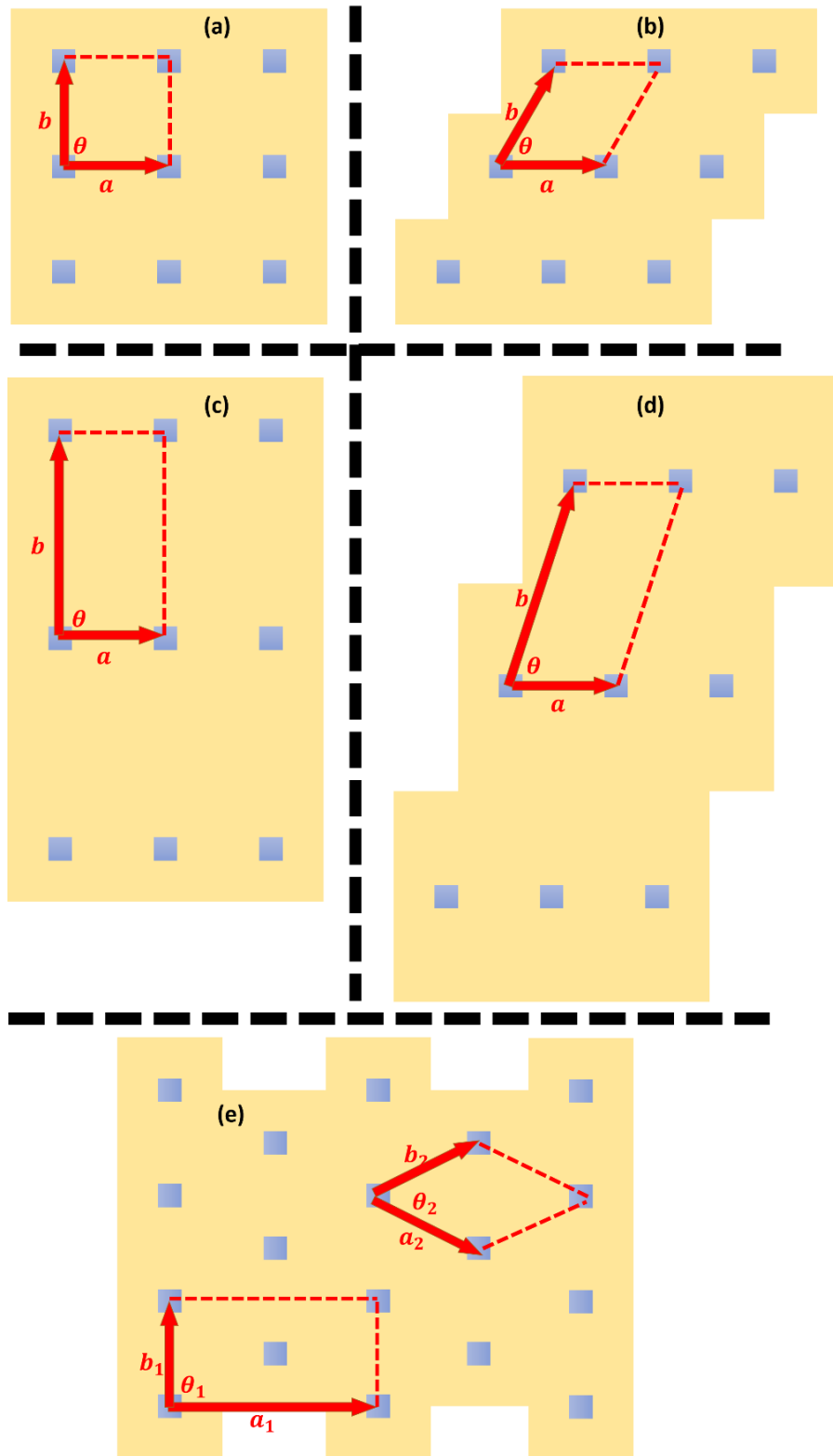
Figure 2.5 – The direct lattices in two dimensional systems including: (a) square, (b) triangular, (c) rectangular, (d) oblique, (e) centered rectangular/rhombus.

Construction of PnC band diagram is often based on the periodicity direction of the phononic crystal structures. Periodic structures can be assumed as repeated direct lattices. The number of ways to produce periodic structures is unlimited. However, when the periodic structures are transferred into direct lattices in two dimensional PnCs, there is only 5 point lattices that define the crystallization/orientation of the structure. These direct lattices are generally referred as square, rectangular, triangular, oblique, rhombus/centered rectangular as depicted in Figure 2.5. The most commonly used 2D PnCs are the square direct lattice. Such designs have been implemented in MEMS resonators frequently and have proven to increase the quality factor of the suspended structures [25-29]. These designs are very suitable to be placed within the MEMS resonators anchors. Since construction solid/air PnCs are favorable for MEMS fabrication because it can be done in one step when releasing the structures, most of the MEMS researchers have utilized the solid/air PnCs due to its microfabrication simplicity to proof the PnCs concept [26-29]. The main approach in this research is to utilize 2D solid-solid PnCs and implement it in MEMS released resonator, which have never been demonstrated yet to the author's knowledge.

2.5 3D PnCs

The 3D PnCs structures are very complicated structure to analyze and fabricate especially in micro-scale sizes. They have 14 direct lattices, which is also called Bravais lattices named after the French physicist who pioneered the study in crystalline systems [65]. In fact, since PnCs is a relatively new topic in acoustics field, most of the designs are based on 2D PnCs. However, the preliminary studies of 3D PnCs were conducted by researchers by numerical simulation, since building 3D periodic structures with two different materials, especially if they are liquid like fluid-fluid PnCs, are very difficult to achieve particularly in microfabrication [66-67]. Investigation of such 3D PnC structures are still open and of interest to macro-scale structures, but the fact that it

is hard to be microfabricated and miniaturized have lowered the interests of these type of PnCs in MEMS field as compared 2D PnCs [67].

2.6 Brillouin Zone

One of the main advantages of PnCs is the fact that they can generate a phononic bandgap, where PnCs can effectively manipulate the sound waves. Similar to its electromagnetic counterparts, the band gap in PnCs forbids sound phonons from propagating within the crystal. The band gap diagram is constructed using the dispersion relation equation, which is frequency dependent on the k vector. These k vectors are wave vectors for the electromagnetic and/or acoustic waves, which are also called Bloch vectors. The overall field takes on the same periodicity of the periodic structures that it passes through [62]

$$E(r) = \psi(r) * e^{i\boldsymbol{k}\cdot r} \tag{2.13}$$

Equation (10) is known as Bloch theorem where $\psi(r)$ is the amplitude function that takes on the same periodicity of the periodic structures and $e^{(ik\cdot r)}$ is the plane wave function that depends on the k vectors but does not have the same periodicity of the periodic structures since it is extracted and analyzed out of one cell.

In periodic structures, in order to plot this dispersion relation, a single crystal (or unit cell) of the periodic crystals is studied individually and analyzed geometrically. Periodic structures, such as PtCs and PnCs, have corresponding direct lattices that simplifies cells repetition as demonstrated in Figure 2.6. A direct lattice is made of vectors that are directed to the other repeated cells in different dimensions based on the two dimensional systems. Let's assume the square direct lattice represents the PnCs repetition as shown in Figure 2.5(a), the vectors that are generated from one cell to another cell generate what are called primitive vectors, which allows the translation of lattices from direct lattices to reciprocal lattices.

Let's assume X is the reciprocal lattice wave vectors [62].

$$X = n_1 b_1 + n_2 b_2 \tag{2.14}$$

where, n are the integers and b are the reciprocal lattice wave vectors [62].

$$b_1 = 2\pi \frac{a_2 \times \hat{z}}{a_1 \cdot (a_2 \times \hat{z})} \tag{2.15}$$

$$b_2 = 2\pi \frac{a_1 \times \hat{z}}{a_1 \cdot (a_2 \times \hat{z})} \tag{2.16}$$

where, z is the 90 degree rotational matrix and a_1 and a_2 are the direct lattice vectors. Table 2.1 shows the primitive vectors results for direct and reciprocal square lattice.

Table 2.1 – Direct lattices and reciprocal lattice primitive vectors of square lattice

	Primitive Vectors	
	Direct Lattice	Reciprocal Lattice
Square Lattice	$a_1 = a\hat{x}$	$b_1 = \dfrac{2\pi}{a}\hat{x}$
	$a_2 = a\hat{y}$	$b_2 = \dfrac{2\pi}{a}\hat{y}$
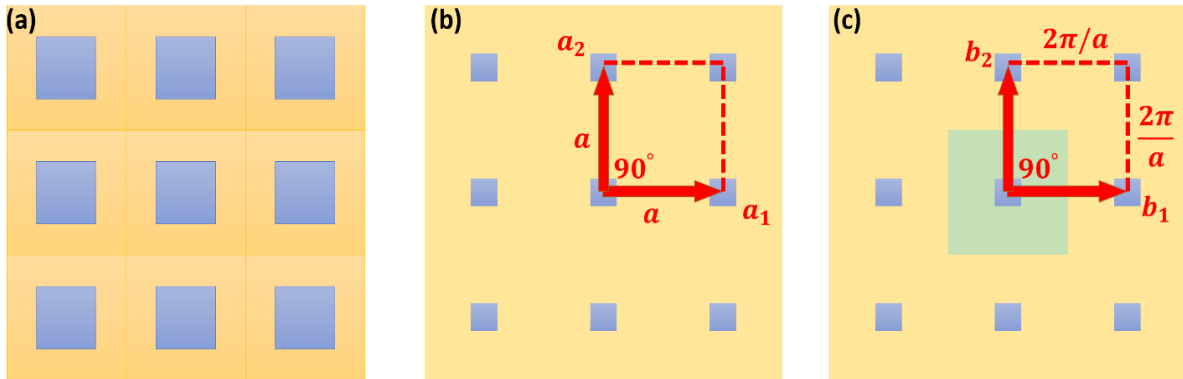
Figure 2.6 – Illustration of (a) periodic structures, (b) direct lattices, and (c) reciprocal lattices.

After plotting the reciprocal lattice, the Brillouin zone of the PnCs structure can be constructed. The evaluation of the dispersion relation takes into account the k vectors in a complete lope of irreducible Brillouin zone. Figure 2.7 shows the Brillouin zone and irreducible Brillouin zone which is the smallest zone where there is no more symmetry.

23
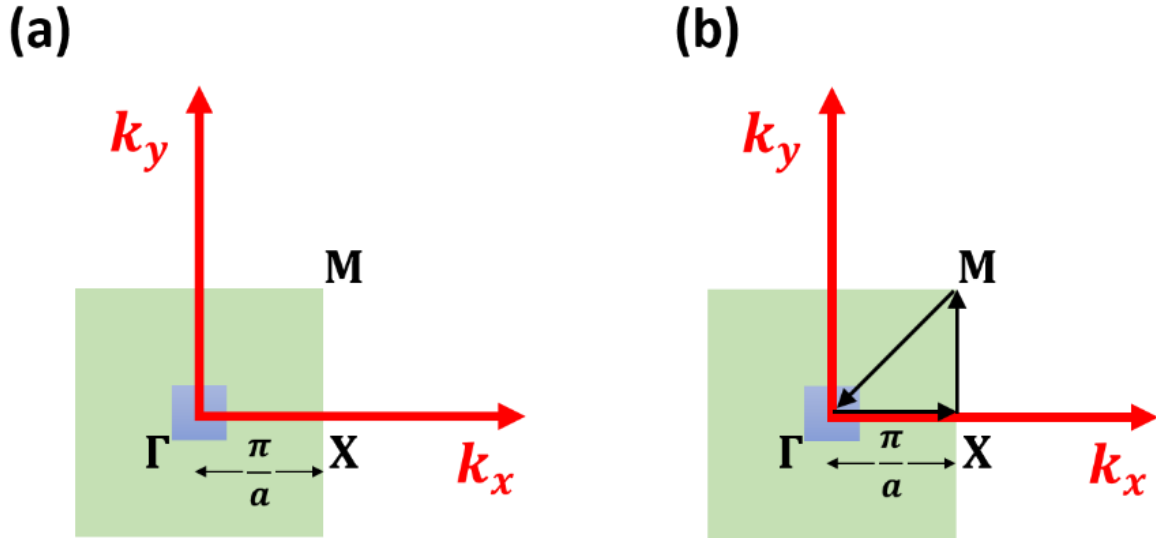
Figure 2.7 – Illustration of reciprocal lattice including (a) Brillouin Zone, and (b) Irreducible Brillouin Zone.

Then, k_x and k_y vectors are solved for many points in (Γ-X-M-Γ) lope [62]

$$\begin{matrix} & \Gamma & X & M & \Gamma \\ k = \begin{cases} k_x \\ k_y \end{cases} = \begin{cases} 0 \dots\dots\dots\dots\pi/2 \dots\dots\dots\dots\pi/2 \dots\dots\dots\dots 0 \\ \hline 0 \dots\dots\dots\dots 0 \dots\dots\dots\dots\pi/2 \dots\dots\dots\dots 0 \end{cases} \end{matrix}$$ (2.17)

Finally, we solve for the overall band diagram using the irreducible Brillouin zone by calculating the eigenvalues at each point of the wave vectors. Plotting the band diagram helps to assess the bands locations and define the existence of the band gaps. By evaluating the Eigen frequencies along the k vectors, the dispersion relation can be determined for examining the band gaps of the structures as shown in Figure 2.8. The high and low acoustic impedance in Figure 2.8 were chosen as silicon dioxide (SiO_2) and Tungsten (W), respectively. These two materials are chosen widely in MEMS devices since they give a very high acoustic mismatch as compared to other materials as illustrated in Table 2.2.
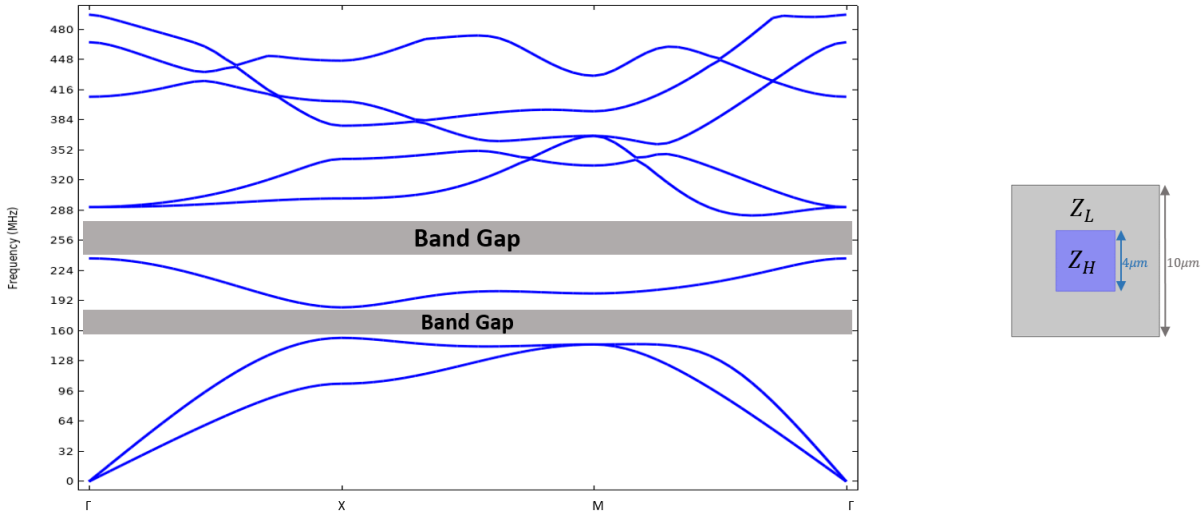
Figure 2.8 – Illustration of (a) Band Gap diagram, and (b) a 2D PnC unit cell that is composed of high and low acoustic impedance materials.

2.7 PnCs Materials

Different field of studies commonly require specific properties for the application of interest. For instance, PtC applications depends highly on light manipulation and reflection, in which materials with relatively high and low refractive indexes are used for such applications. In contrast, PnC applications depends on elastic and acoustic wave reflections, therefore materials with dissimilar high and low acoustic impedances are desired for PnC applications that manipulate the acoustic wave. Previously, such materials with mismatched acoustic impedances are known to be used in commercial SMR designs [68].The acoustic impedance is linearly dependent on the Young's modulus and density of the materials as shown in equation 7. Table 2.2 compares some state-of-the-art material choices that can be used in MEMS devices and their acoustic properties. In this work, silicon (Si) and tungsten (W) were selected strategically to produce relatively low and high acoustic impedances, respectively. And the designs with Si/W solid-solid PnCs are fabricated on silicon-on-insulator (SOI) wafers.

Table 2.2 – PnCs materials choice comparison to several state-of-the-arts

Device	Materials	Impedance Characteristics	E (GPa)	ρ (kg/m^3)	$\dfrac{Z_H}{Z_L}$
SMR[50]	SiO2	Low (L)	70	2200	2.6
	AlN	High (H)	330	3260	
SMR[69]	SiO2	Low (L)	70	2200	7
	W	High (H)	411	19350	
SAW[21]	SiO2	Low (L)	70	2200	7
	W	High (H)	411	19350	
Unreleased BAW[63]	SiO2	Low (L)	70	2200	1.5
	Si	High (H)	170	2330	
Released BAW (This work)	Si	Low (L)	170	2330	4.5
	W	High (H)	411	19350	

2.8 PnCs Designs

In this work, several designs of Si/W solid-solid PnCs were incorporated within thin film piezoelectric transducer on silicon (TPoS) resonators. The comparison between the effects of one and two dimensional PnCs in reflecting the acoustic wave leakage through the anchors will be systematically investigated. The devices were designed, fabricated and tested on SOI wafers. Figure 2.9 shows some samples of the PnCs structures and one implementation of PnCs in TPoS resonator in its CAD layout is shown in Figure 2.10. Figure 2.10 presents one of the TPoS lateral extensional resonator devices with built-in Si/W solid-solid 2D PnCs, which consists of 6 photo lithography mask layers. The microfabrication details of such devices will be discussed in later chapters.
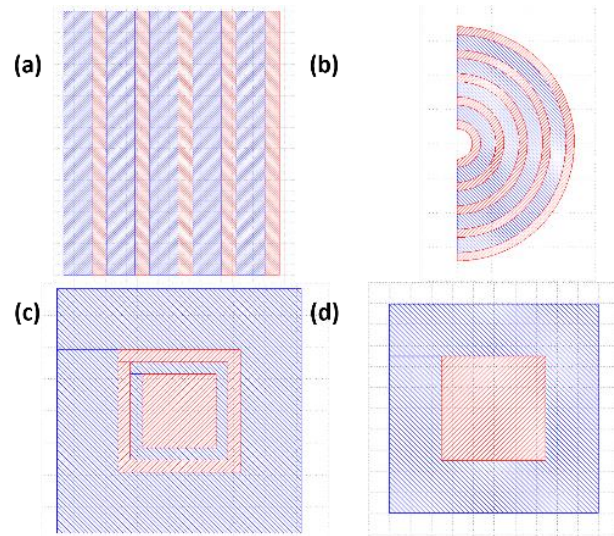
Figure 2.9 – Illustration of several sample PnC designs based on low and high acoustic impedance solid-solid interfaces made of silicon (blue) and tungsten (red) including (a,b) one dimensional PnC, and (c,d) two dimensional PnC.
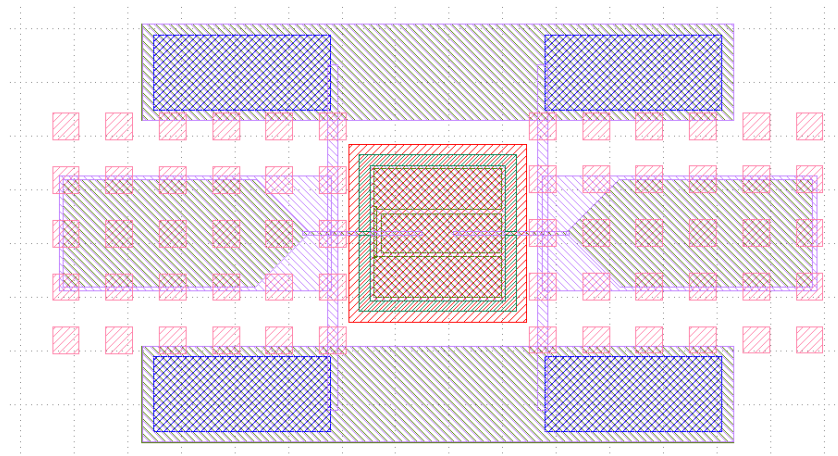
Figure 2.10 – A typical CAD mask layout of a TPoS device with built-in 2D PnCs.

2.9 MEMS Quality Factor

Perhaps, the most defining factor in MEMS resonators performance is their ability to confine the energy within the device structure which is commonly represented by the figure of merits (FOM) of MEMS resonators. For electrostatically transduced resonators, the most frequently used FOM is $f.Q$ product while the $k_{eff}^2.Q$ product is viewed as the FOM for piezoelectrically transduced resonators. Many research groups are aiming in improving the Q

27

(quality factor) using different methods such as special geometrical designs, modified width of anchors or even changing the device materials. To obtain high Q-factor, it is important to understand the energy storage and dissipation mechanisms of the devices. The quality factor is generally defined as the ratio between energy stored and the energy dissipated per cycle [25-29].

$$Q = 2\pi \frac{E_{stored}}{E_{dissipated}} \tag{2.18}$$

The overall quality factor can be determined by a combination of the contributions by all the loss mechanisms in a resonator, which can be expressed as [70]:

$$Q_{total}^{-1} = Q_{air}^{-1} + Q_{material}^{-1} + Q_{anchor}^{-1} \tag{2.19}$$

where, $Q_{air}, Q_{material}$ and Q_{anchor} are the effective quality factors due to dissipations by viscous air damping, material loss, and anchor loss, respectively. The air loss can be suppressed largely by measuring the MEMS resonator devices in vacuum. Due to the nature of having tiny gaps between the electrodes and the resonator body, electrostatically transduced resonators are more strongly affected by air damping which is known as squeeze-film damping effect as compared to the piezoelectrically transduced resonators where the thin film piezoelectric transducer materials are known to be lossy to contribute significant material related losses [64]. Material loss typically occurs either when the acoustic energy is transformed into thermal energy which is known as thermoelastic damping or when the acoustic attenuation coefficient is very minimal which is known as Akheiser loss. Thermoelastic damping occurs due to the heat transfer between the hot and old regions within a resonator when the resonator body goes into compression and tension at different regions during different time of the modal vibration (resonance cycle). The Akheiser loss in piezoelectric transducer materials such as ZnO and AlN is often higher than typical structural materials in MEMS resonators such as Si and diamond [71]. As such, TPoS resonators, where the structural material to piezoelectric material thickness ratio is higher than four, exhibit noticeable

28

better Q factors. Anchor loss is the acoustic energy dissipation through the supporting anchors (or tethers), which has been proven experimentally to limit the Q factor. To overcome this dilemma, the energy leakage through supporting anchor(s) need to be confined to retain high Q's. As such, the study of the acoustic wave reflection has been of utmost interest by MEMS researchers. One way to reflect the acoustic wave back to the resonator is to design quarter wavelength anchor dimension, while positioning them at the nodal points of the resonator, which is a concept that is used frequently in the RF transmission line theory [72]. Another method that was applied in electrostatically transduced resonator with self-aligned anchor is to reflect the acoustic wave using impedance mismatch at the interface between the resonator body and the anchor by leveraging mismatched acoustic impedances between diamond and silicon [64]. The interest is then shifted to the design of special microstructures with acoustic reflection capabilities and implement them in microfabrication technology. PnCs indeed serve this purpose as lots of prior works proved that in recent years [25-29,31-33].

Chapter 3: Development of Thin-Piezo on Silicon (TPoS) Resonators in Single Crystal Wafer with Single-Crystal Silicon Reactive Etched and Metallization (SCREAM) Process

Most of the content of this chapter have already been published [73]. Permission is included in Appendix A.

Radio frequency microelectromechanical systems (RF MEMS) is widely viewed as a potential enabling technology for the multi-standard monolithic transceivers on a single chip with high reliability, high performance and very low (virtually zero) DC power consumption. Among various RF MEMS device components, resonators offer unique benefits because of their very high quality factor, which enables the implementation of advanced functions such as low insertion loss filters, mixer-filters, ultra-low phase noise oscillators and even RF or microwave front-end channel selection for realizing true software defined radios [74-79]. One of the key limitations associated with the RF MEMS resonators is their relatively high motional impedances [79-80], which can be a cumbersome bottleneck against employment of such devices in RF front-end transceivers due to the large impedance mismatch between the resonators and antenna or other front-end modules. Piezoelectrically transduced MEMS resonators have shown its capability on lowering the motional impedance compared to electrostatically transduced resonators [81-82]. In particular, thin-film piezoelectric-on-silicon (TPoS) resonators have been fabricated by using silicon-on-insulator (SOI) wafers, which have shown superior performance as compared to their capacitively transduced counterparts [83-85]. Also, the piezoelectrically transduced TPoS resonators enabled by the SOI technology are capable of operating at frequencies up to a few GHz and retaining its performance reliability [83-86]. SOI wafers provide uniform silicon device layer and buried oxide

layer thicknesses across the whole substrate. However, SOI substrates are quite costly with their prices typically over 150 USD per wafer depending on the specifications. This chapter will cover the fundamental of TPoS resonator, fabrication process and the introducing single-crystal silicon reactive etched RF MEMS resonators.

3.1 TPoS Resonators

Thin film piezoelectric transducers have demonstrated higher electromechanical coupling coefficients while holding slightly higher material related losses. Therefore, incorporating a low mechanical loss material layer under the piezoelectric layer to store the acoustic energy has shown great promises to exhibit low acoustic losses (high-Q's) and lower motional impedances which is known as TPoS resonators. As seen in Figure 3.1, a typical thin-film piezoelectric-on-substrate (TPoS) MEMS resonator consists of a thin-film piezoelectric transducer sandwiched between the top and bottom metallic electrodes situated on top of a low mechanical loss resonator body made of a substrate material such as silicon or diamond.
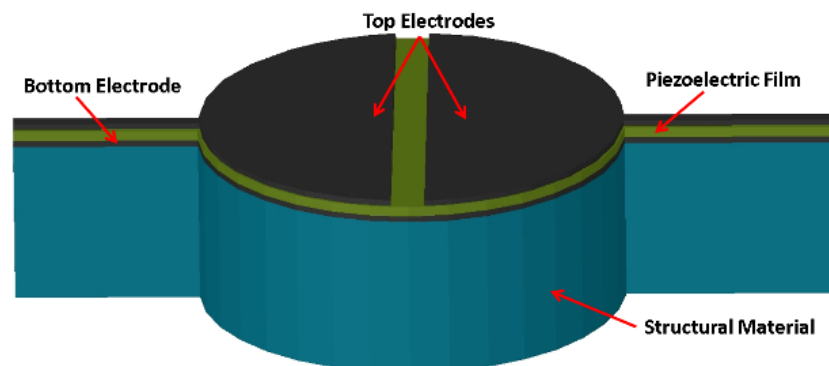
Figure 3.1 – Schematic illustration of electrode and anchor design configurations for a thin-film piezoelectric on substrate (TPoS) disk resonator with electrodes designed for its 1st lateral extensional mode.

The resonance frequency of ZnO-on-Si resonators depends highly on the effective acoustic velocity of the resonator body made of a stack of thin-film ZnO layer and a silicon structural layer as shown in Figure 3.2. The single crystal silicon has a much higher acoustic velocity as compared

to that of sputtered piezoelectric ZnO thin film. Thus, the thicker the Si structural layer is, the higher the resonance frequency would be as indicated by the governing equations (3.1) and (3.2) [87-89].

$$v_{eq} = \sqrt{\frac{E_p T_p + E_{top} T_{top} + E_{bott} T_{bott} + E_{dev} T_{dev}}{(\rho_p T_p + \rho_{top} T_{top} + \rho_{bott} T_{bott} + \rho_{dev} T_{dev})(1 - \mu^2)}} \tag{3.1}$$

$$f_0 = \frac{k}{x} v_{eq} \tag{3.2}$$

where k is the lateral mode constant of the resonator; x is the lateral extensional mode characteristic geometrical dimension that could be length, width or radius as shown in Figure 3.1 and Table 3.1; and v_{eq} is the equivalent acoustic velocity of the stacked TPoS resonator structure that is highly dependent on the Young's modulus (*E*), thickness (*T*) and density (*ρ*) of each of the constituent layer of the TPoS resonator body; and an averaged Poisson's ratio (*μ*).
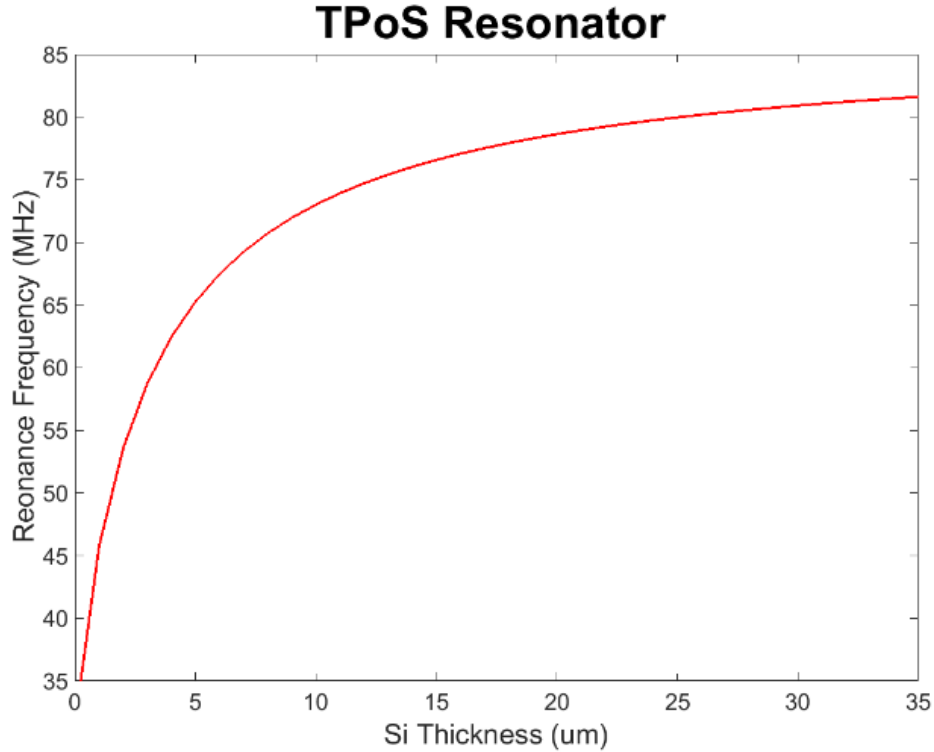
Figure 3.2 – Resonance response with thicker Si layer in of disk TPoS with a radius of 50 um.

Table 3.1 – Lateral mode shapes of plate length extensional and disk extensional.

Mode	Plate Length Extensional	Disk Extensional
1st		
2nd		
3rd		
4th		
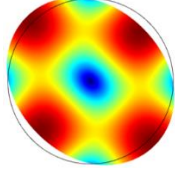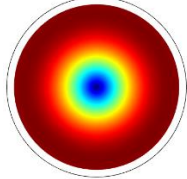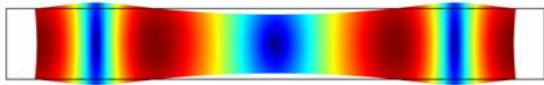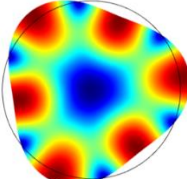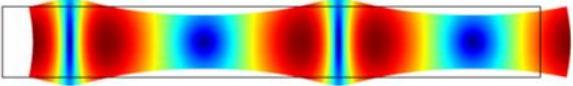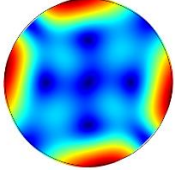
3.2 MEMS Resonators Equivalent Circuit Model

System components in RF MEMS can be converted from electrical to mechanical systems and vice versa. The analogy between the two systems is widely known in suspended devices in microsystems, as shown in Table 3.2 and Figure 3.3, due to the fact that applying conventional mechanical signal (force/pressure) for extremely small devices (nano/micro sizes) are not particular and almost impossible to notice the mechanical response or detect it mechanically. Applying electrical signal, on the other hand, comes really handy since the all it needs is just a connection to the microstructures without harming them. The electrical signal then is converted to a mechanical signal using the piezoelectric material properties in which force the suspended

structure into vibration. Once vibration occurs, the signal is converted reversely to an electrical signal in which is detected at the output.

Table 3.2 – Mechanical and electrical analogies in MEMS systems

Mechanical System	≡	Electrical System
Force F	≡	Voltage V
Velocity $v = \dot{x}$	≡	Current $I = \dot{q}$
Mass M	≡	Inductance L
Compliance $1/k$	≡	Capacitance C
Damping ζ	≡	Resistance R
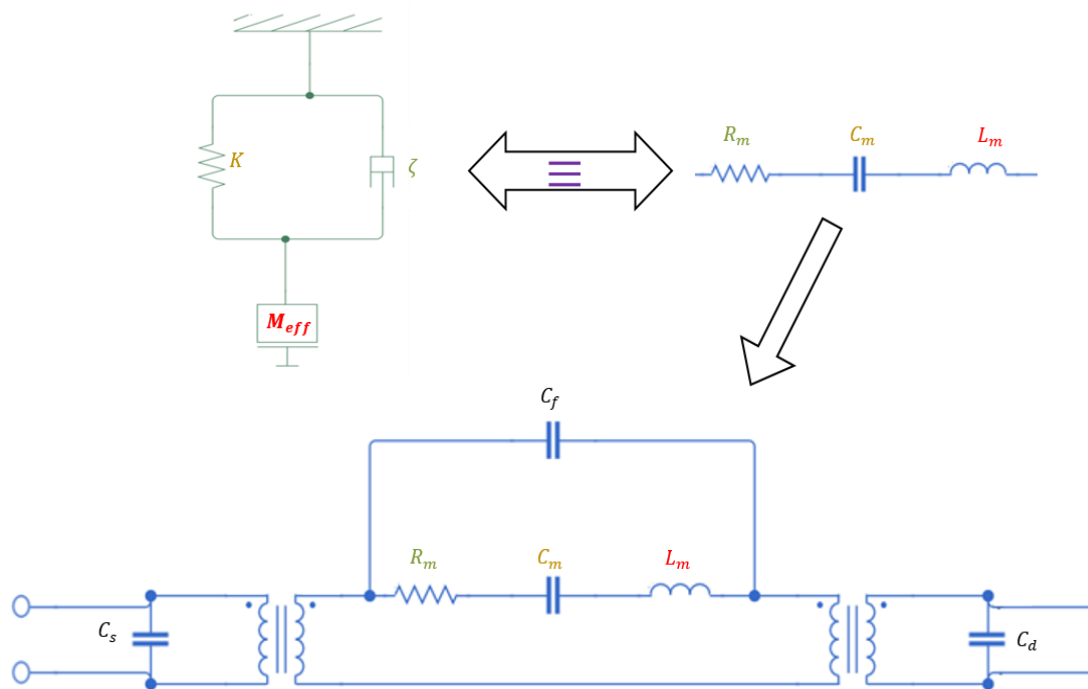
Figure 3.3 – Electrical and mechanical components in MEMS systems.

The circuit model of the vibrating structures in MEMS systems is known Butterworth-Van Dyke (BVD) model. This model is the most widely used model in RF MEMS systems in both electrostatically and piezoelectrically transduced resonators. As can be noticed from Figure 3.3 above, the motional resistance Rm, inductance Lm and capacitance represent the mechanical vibration of the structure while the C_f is the capacitance between the electrodes. The BVD circuit model is a serious LCR in parallel with parasitic capacitance C_f.

34

The relation between the mechanical system elements and electrical elements are given as:

$$R_{\mathrm{m}} = \zeta/n^2 \tag{3.3}$$

$$C_{\mathrm{m}} = n^2/k \tag{3.4}$$

$$L_{\mathrm{m}} = m/n^2 \tag{3.5}$$

where, n^2 are the transduction factors of the input and output terminals. The serious resonance in the BVD model is given by:

$$f_{\mathrm{s}} = \frac{1}{2\pi\sqrt{L_m C_m}} \tag{3.6}$$

while, the parallel resonance is:

$$f_{\mathrm{p}} = \frac{1}{2\pi\sqrt{L_m \dfrac{1}{C_m^{-1} + C_f^{-1}}}} \tag{3.7}$$

3.3 Fabrication of ZnO Thin-Film Piezoelectric-on-Substrate (TPoS) Resonator

Typical TPoS resonators consists of device structure layer underneath the piezo with the metallic layers that serve as bottom and top electrodes. TPoS fabrication process mostly requires a silicon-on-insulator (SOI) substrate as a starting substrate. The fabrication can start with pre-released to the devices before building the stack layers or final back side release after the stack layers. Figure 3.4 shows the possible release ways to fabricate TPoS. TPoS requires typically 5 microfabrication masks; four masks for defining the structure layers and the resonator body. In addition, a released mask layer to suspend the TPoS devices can be performed at the beginning the fabrication process which is known as pre-release process or at the end as a last step by back releasing the micro-resonators structures. Fabrication process details of the resonator mask layers will be discussed in the next section while the release of TPoS resonators will be discussed in the PnCs fabrication chapter.
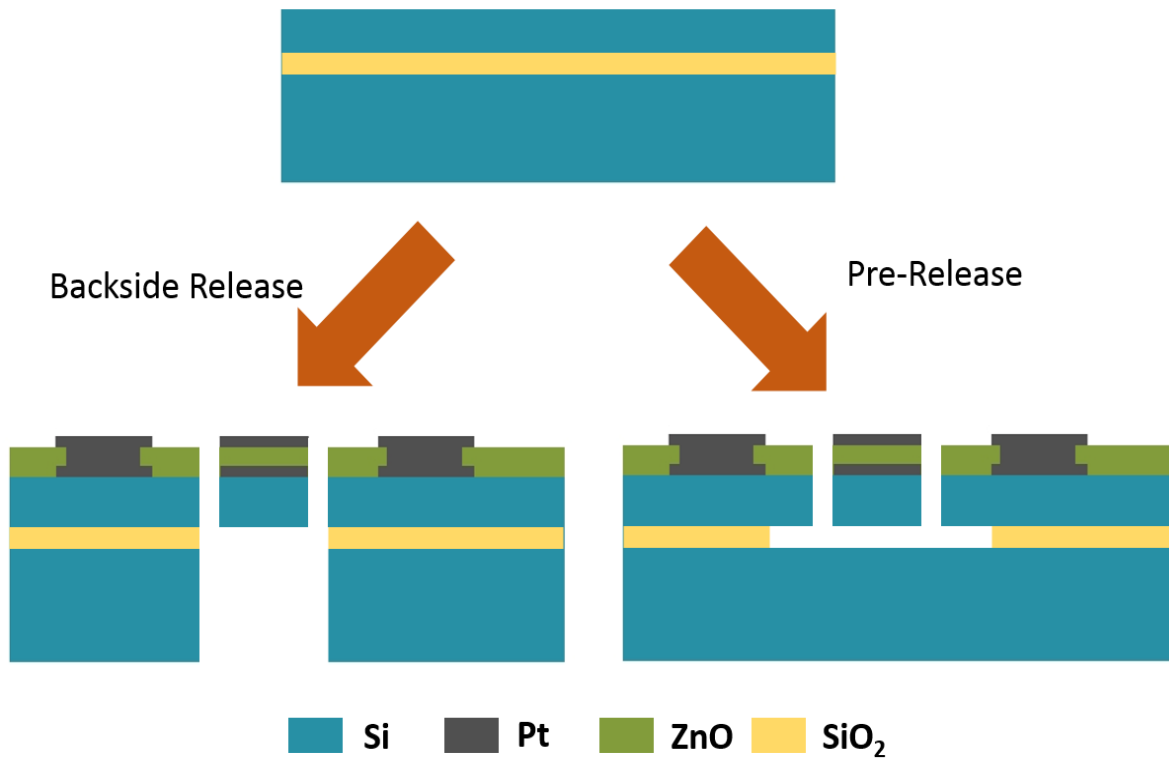
Figure 3.4 – Typical TPoS devices fabrication process begins with SOI wafer and released using backside release or pre-release process.

3.4 Thin-Piezo on Single-Crystal Silicon Reactive Etched RF MEMS Resonators

This section demonstrates how a single crystal silicon wafer can be used to fabricate thin film piezoelectric-on-silicon (TPoS) resonators by utilizing a modified version of Single Crystal Silicon Reactive Etch and Metallization (SCREAM) process. The developed process enables the fabrication of MEMS resonators with varied device layer thicknesses ranging from sub-micrometer to tens of micrometers (one thickness per die) from in a single bulk silicon wafer, while avoiding the need of costly silicon-on-insulator (SOI) substrates. The thin-film piezoelectric on single-crystal silicon reactive etched technique allows batch fabrication of TPoS resonators, while also retaining the same number of photolithography steps. Figure 3.5 presents the step-by-step fabrication process flow of piezoelectrically-transduced lateral extensional resonator with the

first four photolithography steps before the final releasing, which will be discussed subsequently.

The fabrication process begins with a photolithography and lift-off process to pattern the bottom electrode over a 4 kΩ.cm high-resistivity silicon wafer, which is composed of sputtered 40nm Cr and 200 nm Pt as seen in Figure 3.5 (a). Then, a reactive sputtering of 500 nm of ZnO is performed with optimized parameters to achieve a (002) c-axis aligned crystal orientation as seen in Figure 3.5 (b). A via hole to connect to the bottom ground electrode is formed by a photolithography and ZnO wet etching using 1 HCL:100 H_2O as seen in Figure 3.5 (c). The top electrode made of 40nm Cr/ 200nm Pt is thereafter defined by a photolithography and lift-off process before patterning the resonator body. Finally, a ZnO reactive ion etching (RIE) recipe with 30 sccm CH_4, 16 sccm Ar and 8 sccm He gas reactants is used to define the resonator body shape by selectively etching ZnO to reach the surface of the Si substrate as shown in Figure 3.5(e).
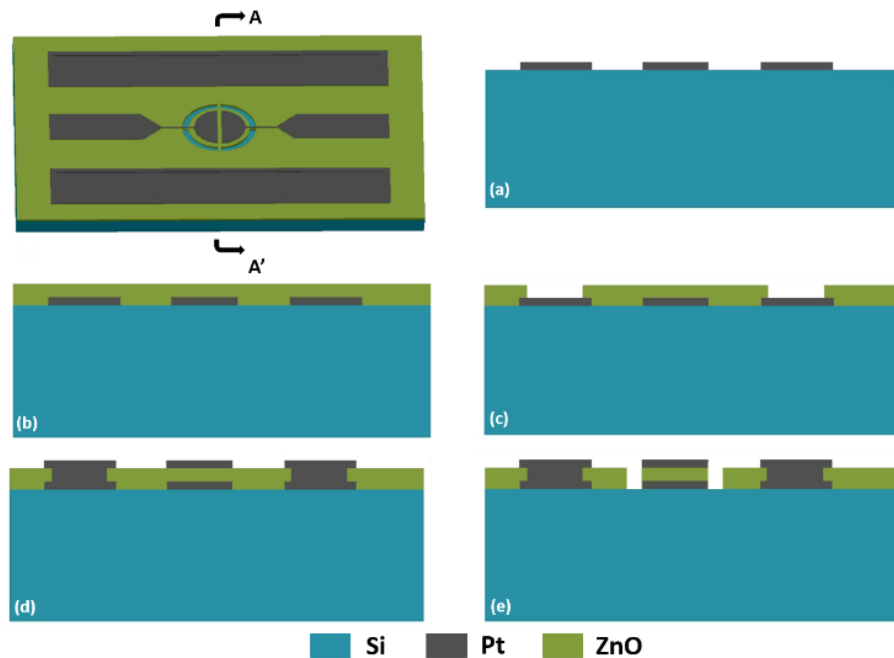
Figure 3.5 – Step-by-step illustration of the fabrication process flow of piezoelectrically-transduced lateral extensional mode resonators including: (a) bottom electrode lift-off process; (b) reactive sputtering of c-axis aligned ZnO piezoelectric film; (c) via opening by ZnO wet etching; (d) top electrode lift-off process; (e) patterning of the resonator body by RIE etching.

37

The dry releasing process of such devices can be realized by using the high aspect ratio deep reactive ion etching (HAR DRIE), which enable dry etching into the silicon substrate to define the thickness of the silicon device layer as the resonator body. As shown in Figure 3.6, the HAR DRIE starts immediately after the ZnO piezo-transducer layer is defined by RIE etching. Then a highly conformal layer of 40nm-thick aluminum oxide (Al_2O_3) is deposited by atomic layer deposition (ALD) to cover and protect the sidewall of the etched silicon trenches (the contour of resonator body) during subsequent silicon dry etching. The last step is to release and suspend the resonators by using a pure SF_6 based silicon isotropic dry etching process, after removing the ALD Al_2O_3 hard mask layer solely from the exposed horizontal surfaces by a directional dry etching.
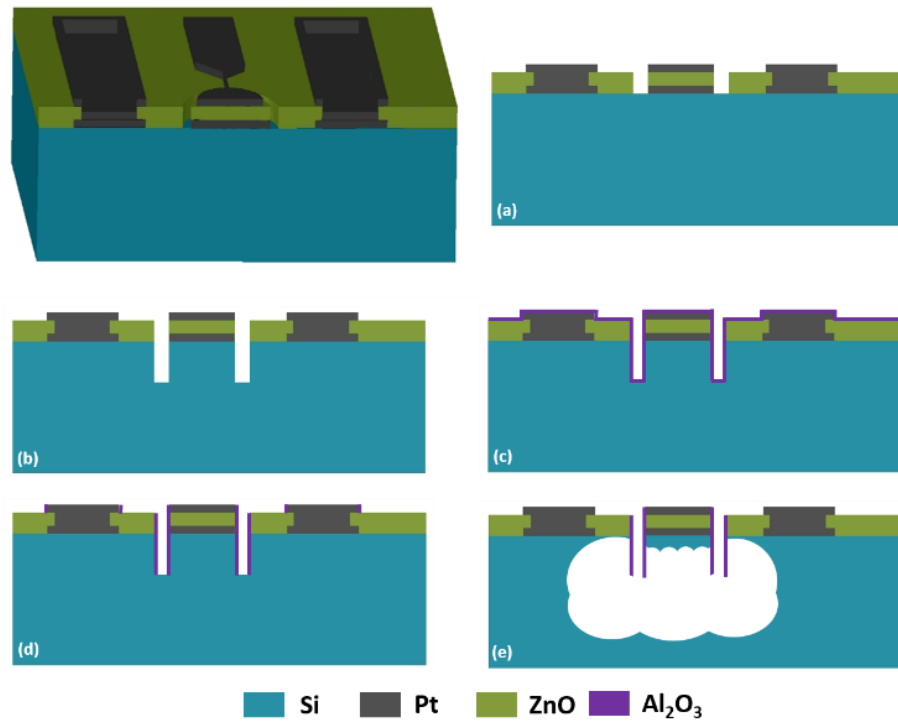
Figure 3.6 – Step-by-step illustration of the release process technique including: (a) patterning of ZnO transducer; (b) high aspect ratio Si DRIE etch to define the resonator body; (c) ALD deposition of Al_2O_3 sidewall protection layer; (d) directional dry etching of Al_2O_3 layer on all exposed horizontal surfaces; (e) Si isotropic etch to release all thin-film piezoelectric-on-silicon resonator devices.

Silicon isotropic and anisotropic reactive ion etching etch rate depends on both the number of free F radicals and the total amount of exposed silicon surfaces. Consequently, the narrower opening surrounding the resonator body for release results in slower silicon etch rate [90]. The DRIE anisotropic etch rate decreases with etching time as the etch depth and the resultant aspect ratio of the etched trenches increase, thus requiring more time for SF_6 reactant to reach the bottom of the trench and the etch-generated byproducts to exist [91-95]. The thickness control of the TPoS resonator substrate layer in silicon starts with knowing the exact etch rate and profile of the SF6 isotropic silicon releasing process. Then, some extra depth is added to the DRIE etched trench to compensate for the known amount of silicon device layer that will be removed during the isotropic release to ensure a uniform Si device layer underneath the ZnO piezoelectric transducer layer. In general, the etched trench depth by a high-aspect-ratio DRIE process is typically increased by a factor of roughly three times of the desired silicon device layer thickness that also depends on the resonator lateral dimensions and the trench opening sizes. As an overarching goal, the TPoS devices with different silicon device layer thicknesses were fabricated from a single 4-inch wafer. Firstly, the wafer was diced into about 10 dies that are 20mm each. The modified process of varied release process conditions (i.e., duration of anisotropic and isotropic silicon etching) were applied on each die to obtain different Si device layer thicknesses. The desired silicon device layer thicknesses can be obtained by anisotropic etching through the trench opening with a depth of roughly three times of the desired Si device layer thickness by using a high-aspect-ratio DRIE or Bosch process. It is observed that the etch rate of the pure SF_6 based isotropic silicon RIE process for releasing the TPoS devices vary from 6um/min to 12um/min depending on the sizes of the release opening and the width of the trench as shown in Figure 3.7 [96-98].
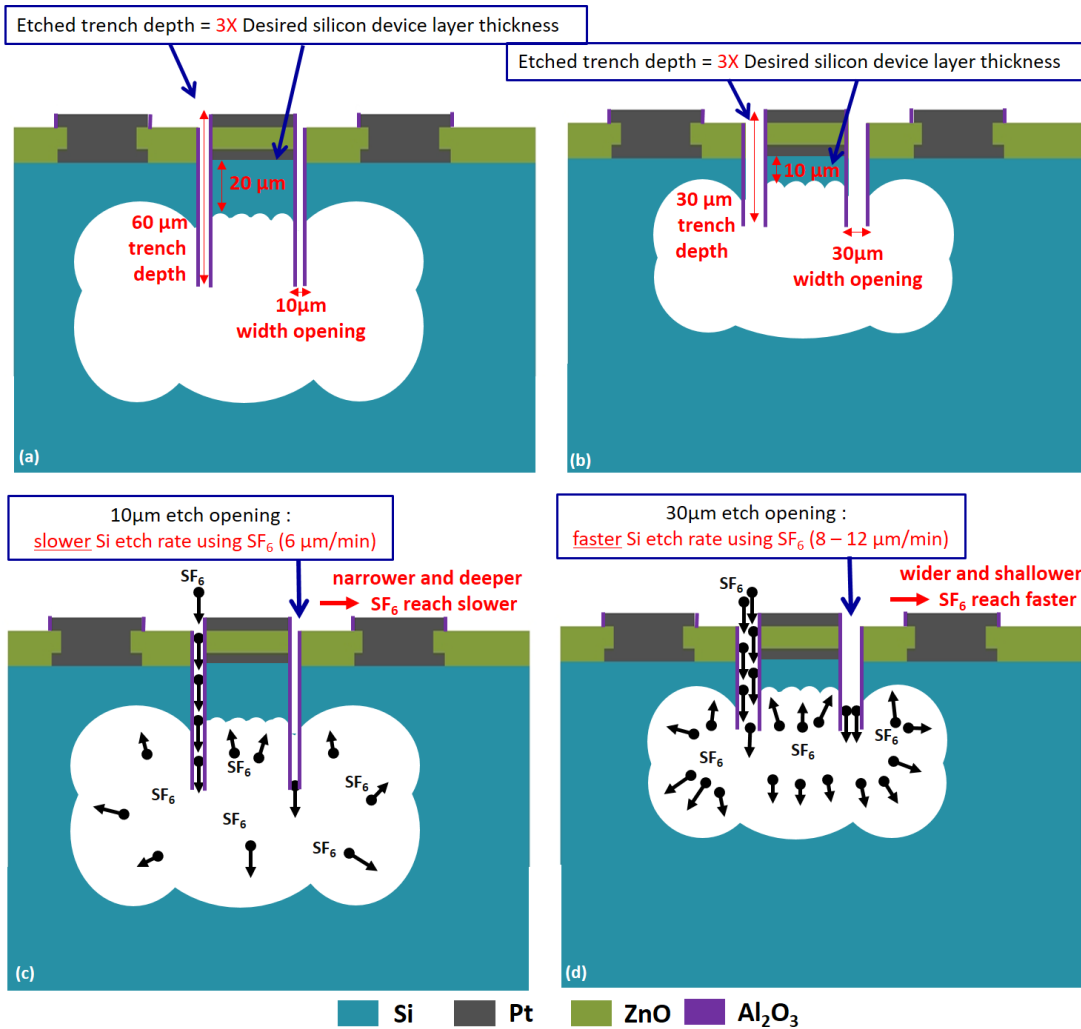
Figure 3.7 – Cross-sectional diagram of a combination of anisotropic etching (DRIE) and isotropic etching of silicon to achieve the desired device layer thickness: including (a) a device with a 20um Si device layer after a 60um anisotropic trench depth; (b) a 10um Si device layer after a 30um anisotropic trench depth; (c) an illustration of narrower and deeper trench opening that results in slower Si isotropic etch rate; and (d) a wider and shallower trench opening that results in faster Si isotropic etch rate.

Figure 3.8 shows measured frequency responses of two ZnO-on-Si TPoS resonators with different resonator mode designs. As shown, a ZnO-on-Si disk resonator operating in its 1st lateral extensional mode has shown an unloaded Q factor as high as 1,567 and a motional impedance (Rm) of 3.93 kΩ, whereas a rectangular-plate device operating in its 10th lateral width extensional mode has exhibited an unloaded Q of 1,013 and a fairly low motional impedance (Rm) of 791 Ω

as seen in Figure 3.8 (b). Table 3.3 summarizes the key measured performance parameters for the first four lateral extensional modes of a few fabricated resonators with varied Si thicknesses.
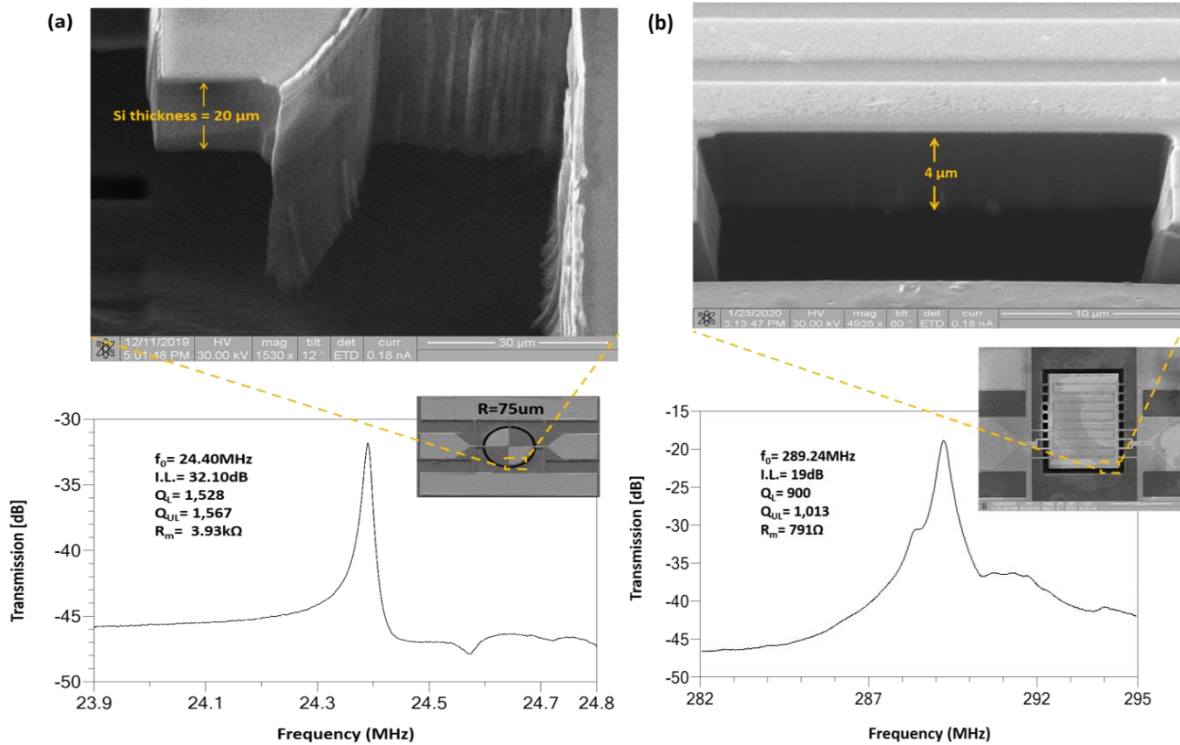
Figure 3.8 – Measured frequency responses: (a) a released ZnO-on-Si 1st lateral extensional mode disk resonator with a radius of 75μm and a Si device layer thickness of 20μm; (b) a released ZnO-on-Si 10th lateral extensional mode resonators with a 96μm wide rectangular plate and a Si device layer thickness of 4μm.

Figure 3.9 shows measured broadband frequency characteristics of a 75μm-radius disk resonator with a 4μm-thick Si device layer by including the first four lateral extensional modes. As expected, much stronger resonance peaks were observed for the first and fourth modes as compared to the second and the third modes due to the anchor placement (reduced anchor related losses) and the top electrode design implementation. The fourth lateral extensional mode of disk resonators is used to evaluate the overall device performance parameters, such as resonance frequency, quality factor, and motional impedance, since this mode is anticipated to exhibit the highest Q's amongst first four lateral extensional modes based on our prior work [99].
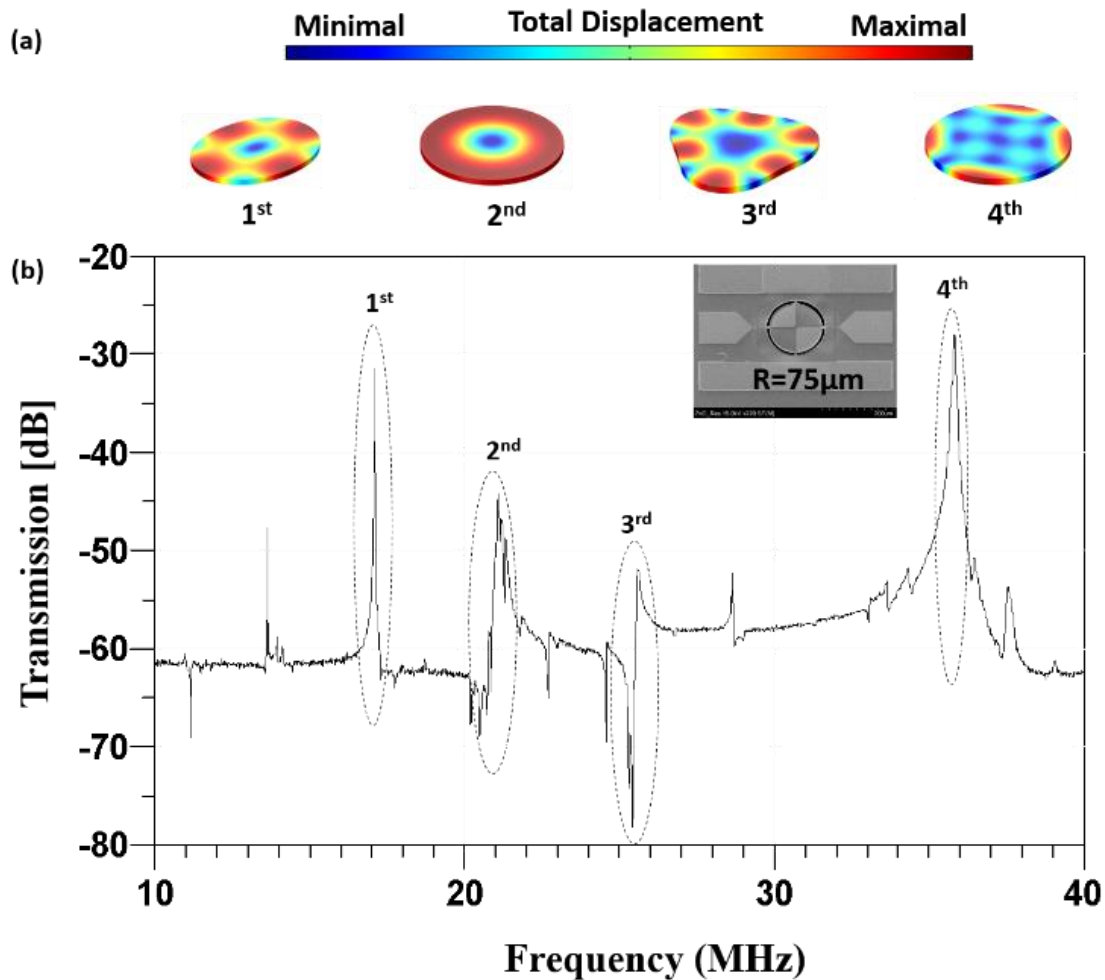
Figure 3.9 – (a) Simulated mode shapes of the first four lateral extensional modes of a disk resonator by COMSOL finite element modal analysis; and (b) measured frequency response of a released 75µm radius disk resonator with a 4um-thick Si device layer, in which the first four major lateral extensional modes are identified.

Figure 3.10 shows variations of the resonance frequency, insertion loss, Q-factor and motional impedance with respect to the varied Si device layer thickness between 0.1µm and 7µm for ZnO-on-Si disk resonators with a 50µm radius operating at the 4th lateral extensional mode. Figure 3.10 (a) presents measured resonance characteristics versus the varied Si layer thickness, while Figure 3.10 (b) reveals a strong dependence of both quality factor and motional impedance on the chosen silicon device layer thickness due to silicon's superb acoustic energy storing ability. Although they did not exhibit Q-factors as high as those achieved by SOI technology with an

42

identical silicon device layer thickness due to the fabrication constraints and limited Si layer uniformity. Both resonance frequency shift and the motional impedance change have been observed in Figure 3.10 that indicates an optical overall performance can be achieved when a Si device layer thicker than 7µm is used.
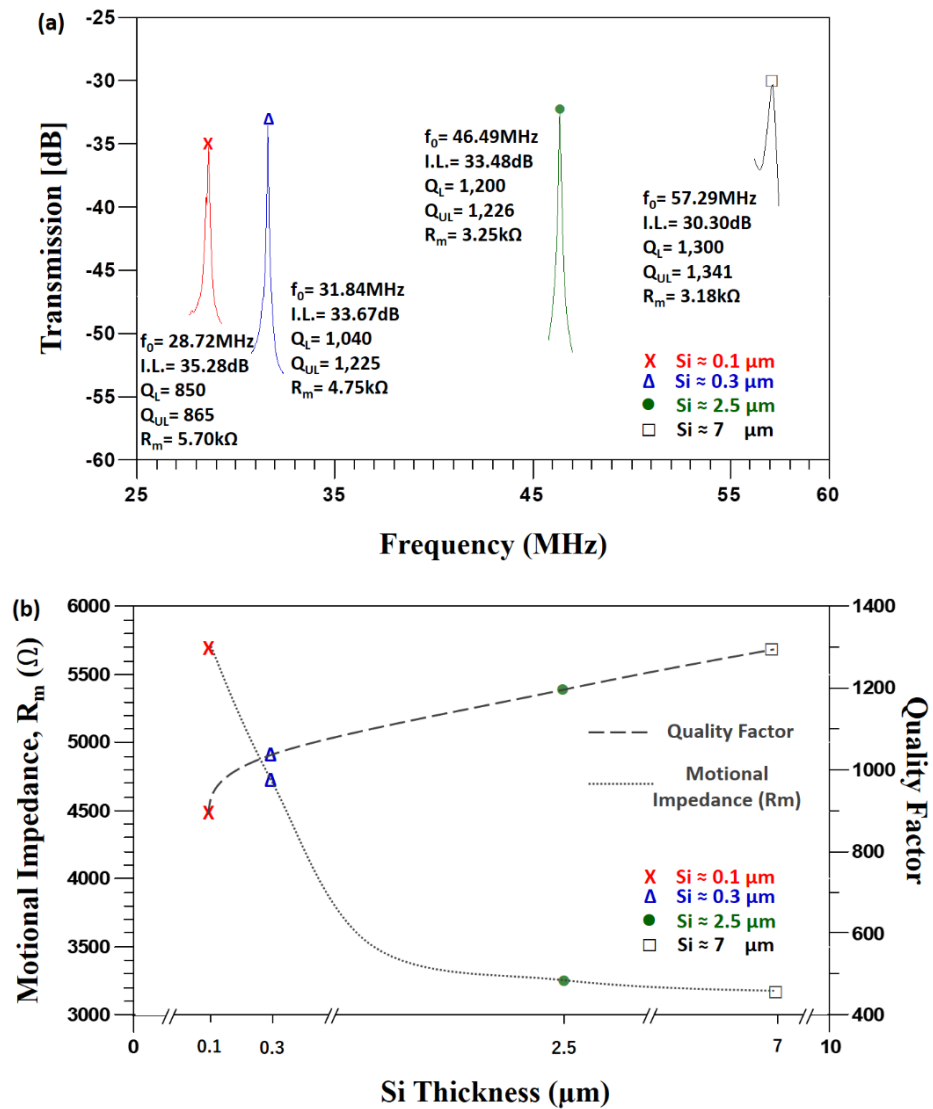
Figure 3.10 – The variations of the resonance frequency, insertion loss, motional impedance, and quality factor versus the varied thicknesses of the Si device layer for identically-sized disk resonators with a 50µm radius operating at the fourth lateral extensional mode.

Figure 3.11 presents normalized motional impedances of several ZnO-on-Si disk resonators with the same 500nm-thick ZnO piezoelectric transducer layer along with varied Si device layer thicknesses between 1um and 45um. As shown, the increase of the Si device layer thickness from 1um to 20um lowers the motional impedance gradually, followed by a drastic rise of the motional impedance when the Si layer thickness gets above 20um.
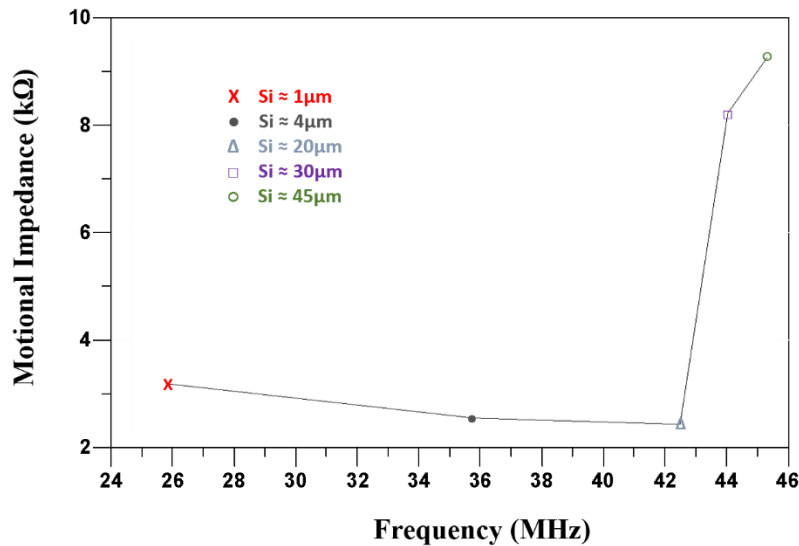
Figure 3.11 – Normalized motional impedances of several identically sized ZnO-on-Si disk resonators with 75µm radius and varied silicon device layer thickness operating at the 4th lateral extensional mode.

The modified process technique has demonstrated some initial promises for fabrication of TPoS resonators with process-specified Si device layer thickness over diced substrates from a single Si wafer. The preliminary results have shown quite promising frequency characteristics of the released resonators in terms of the measured unloaded Q and motional impedance without using the more costly SOI technology. Moreover, some of the process parameters can be further improved and a HF-etch resistant piezoelectric material, such as AlN, could be used instead of ZnO to enhance the process yield and allow removal of Al_2O_3 protective layer to reduce induced dissipations [100].

Table 3.3 – Measured results of ZnO-on-Si disk resonators with a radius of 75µm, a 500nm-thick ZnO piezo-transducer layer and varied Si device layer thicknesses ranging from 1µm to 20µm, operating at 1st, 2nd, 3rd and 4th lateral extensional modes

Si thickness	1 µm				4 µm				20 µm			
Modes	1st	2nd	3rd	4th	1st	2nd	3rd	4th	1st	2nd	3rd	4th
f_0 (MHz)	12.74	15.69	19.42	25.85	17.08	21.12	25.54	35.8	24.4	32.8	36.41	42.5
$I.L.$ (dB)	32.66	42.43	52.3	30.4	32.12	43.25	52.03	28.54	32.1	35.35	33.4	28.15
Q_L	1228	344	300	490	1520	387	502	419	1528	804	805	980
Q_{UL}	1257	347	300.7	505	1559	389.68	503.26	435.28	1567	818	823	1020
R_m (kΩ)	4.2	13.13	41.11	3.21	3.94	14.43	39.84	2.57	3.93	5.76	4.58	2.46

Chapter 4: Solid/Solid PnCs Fabrication Process in TPoS Resonators

The microfabrication process of PnCs depends on the nature of the material. For instance, Air/Solid PnCs in SAW devices don't require refilling of etched holes unlike solid/solid PnCs, where etched holes have to be made and refilled by processing [21]. Similarly, BAW devices equipped with PnCs are typically designed with both the resonator body and PnCs constructed simultaneously. In this chapter, the fabrication process of the solid/solid PnCs in SOI wafers will be discussed in detail.

4.1 Material Selections

PnCs material selection was discussed earlier in Chapter 3, however fabrication methodology requires special design and processing techniques due to the needed micro-scale dimensions. As mentioned earlier, silicon and tungsten were chosen as building materials for the solid/solid PnCs due to their drastically dissimilar acoustic impedances (high and low). Besides their elastic properties that make them promising candidates for acoustic reflection applications, these two materials are also compatible with CMOS IC foundry processing technology and allow for parallel fabrication of CMOS with MEMS systems [24].

In addition, these PnC building materials have to be carefully selected for their compatibility with microfabrication to ensure their dry/wet etchants in subsequent processing steps won't affect any other materials. In microfabrication technology, this could be a dilemma for getting a fully functional device, which will sometimes require the process itself to be modified to overcome such obstacles.

4.2 Lateral BAW Device

The objective of this work is to design thin-film piezoelectric on silicon (TPoS) lateral BAW resonators equipped with strategically designed solid/solid PnCs. Figure 4.1 shows a simplified schematic model of the device used in this work. As can be seen in Figure 4.1, the device has two ports which are connected directly to the vector network analyzer (VNA) for characterization of its frequency characteristics. Testing procedure will be discussed in details in the next chapter. The purpose of the PnCs design is to lower the acoustic losses through the TPoS resonator anchors by reflecting the acoustic waves thus achieving higher quality factor. As such, device performance is expected to be significantly improved. Therefore, PnCs need to be designed strategically such that the TPoS device resonance will occur within the PnCs' band gap. Meanwhile, the PnCs need to be placed where the acoustic leakage is expected to occur, which are located at the supporting anchors for TPoS resonator devices.
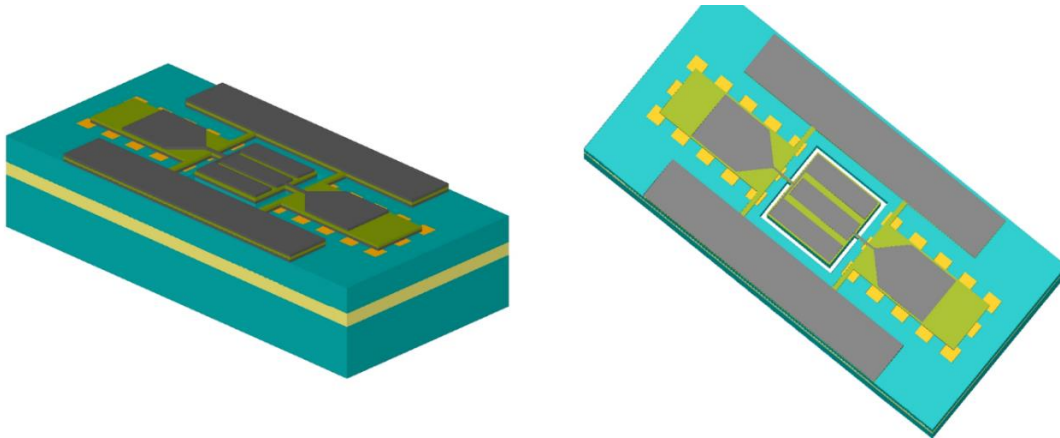
Figure 4.1 – Schematic illustration of the TPoS resonator device model equipped with PnCs in this work at two different angles.

4.3 Fabrication Process

The entire microfabrication process of this work has been done using the on-campus cleanroom facilities at Nanotechnology Research and Education Center (NREC) at University of

South Florida (USF) as shown in Figure 4.2 and Figure 4.3. The process steps utilized in this work include photolithography, wet and dry etching, characterization using X-Ray diffraction (XRD) and scanning electron microscope (SEM). This work starts with design the layout to prepare the photomask for the PnCs as a starting layer with the remaining 5 photo mask layers that are identical to the typical TPoS resonator fabrication over SOI wafers. This process uses the back-side release photomask layer instead of pre-release process.
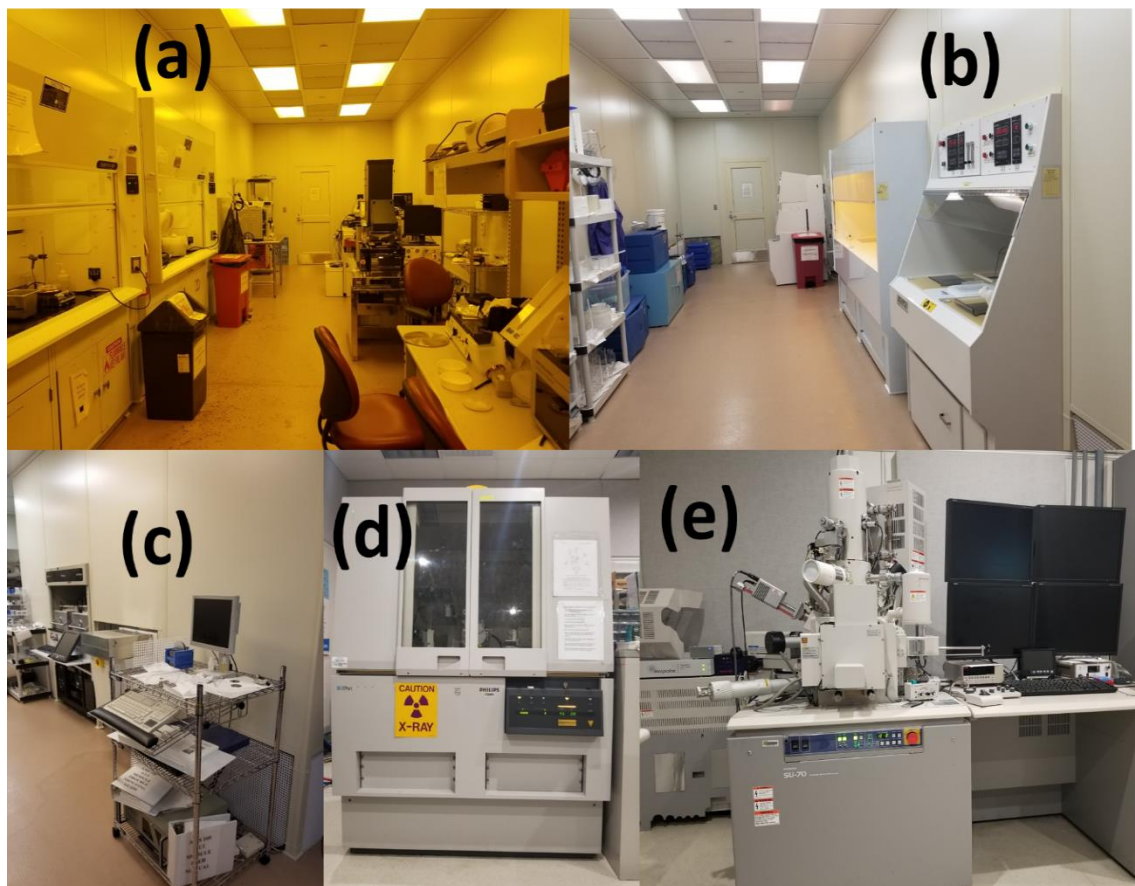
Figure 4.2 – NREC facility microfabrication equipment including: (a) UV lithography bench, (b) chemical wet bench, (C) dry etch systems, (d) XRD, and (e) SEM.

The deposition of the material layers in this work was performed using an AJA Orion 5 ultra-high vacuum (UHV) sputtering system. In addition to the conformability of a larger variety of thin-film materials deposited using the sputtering system, this system in particular has features

such as a substrate heater, a rotational substrate holder chuck, and a pressure valve controller, which allow the user to control the deposited material conditions.

Figure 4.3 – AJA Orion 5 UHV sputtering system.

4.4 PnCs Layer

PnCs structures were micro-fabricated using dry and wet etching methods as well as chemical mechanical polishing (CMP). CMP can be seamlessly incorporated with the solid/solid PnCs microfabrication process flow, however this method poses complexity and uniformity issues across the wafer. In this work, patterning of the PnC microstructures was done through two sequential steps in a single lithography process. An SOI wafer is chosen as the starting substrate, which is etched anisotropically using deep-reactive ion etching (DRIE) to create trenches in the silicon device layer. The SOI substrate properties is important for this process since it determines

the amount of filling required in this process. The buried oxide isolation layer is 2 um and the resistivity of the Si device and substrate layers are 1Ωcm and 20Ωcm, respectively.

After several experimental tests, the lift-off process has shown its capability to etch trenches in the Si and fill them with Tungsten using a bilayer lift-off by using a positive photoresist (AZ1512) on top of a layer of thick lift-off resist (LOR30B). The silicon was etched using standard high aspect ratio (HAR) Bosch DRIE process in an inductively coupled plasma (ICP) etcher for 5-10 seconds for a 2um depth. Then, tungsten was sputtered on the wafer to refill the 2um-depth trenches. Finally, the LOR is removed using AZ400 developer at 60 degrees Celsius as shown in Figure 4.4.
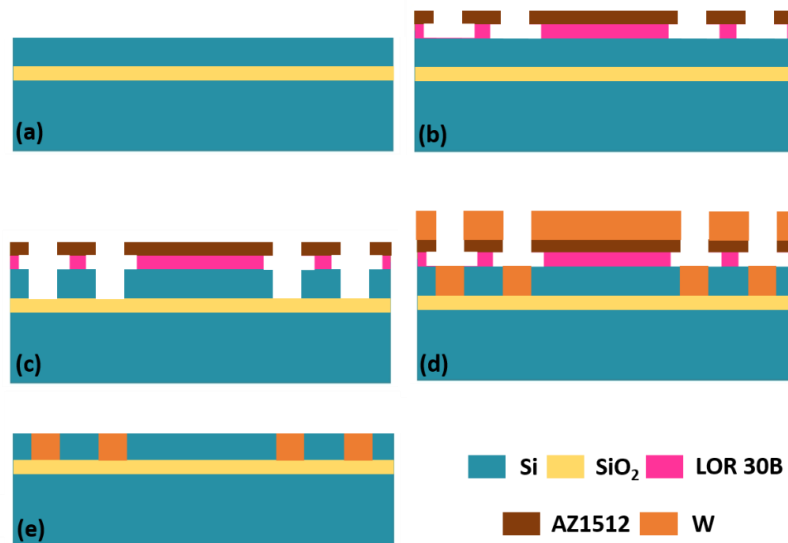
Figure 4.4 – PnCs microfabrication process flow steps, including (a) SOI starting wafer; (b) lift-off lithography using LOR 30B and AZ1512; (c) 10 seconds HAR Si etch for 2um trench depth;(d) tungsten (W) sputtering; (e) lift-off process by removing LOR 30B using AZ400 developer.

The Si/W refilled interface is ideally smooth across the wafer. But due to the nature of microfabrication, it was noticed that Si/W areas were not perfectly smooth but instead have a variation of ~20-60nm in layer thickness which is acceptable as long as it doesn't cause an electrical disconnect for the metal layer in the next process. Due to sputtering process

conformability, values less than half of the bottom electrode thickness should not cause a shortage for the bottom electrode layer. Figure 4.5 shows the cad pictures of the PnCs aligned with the bottom electrode. The thickness and roughness were measured using a profilometer (DekTak 150) as shown in Figure 4.6. If the surface roughness exceeds an acceptable range, the process has to be halted or repeated to prevent further complications.
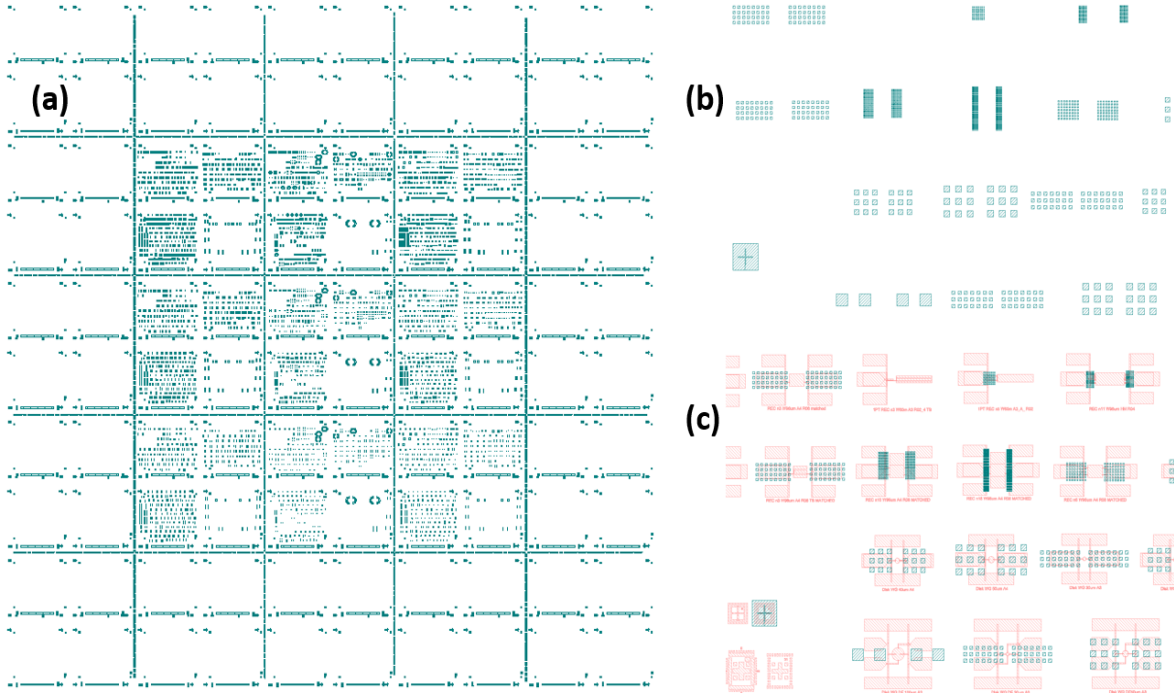
Figure 4.5 – (a) Five inch photomask of tungsten (W) refilled cavity; (b) zoomed-in region of PnC layout; (c) bottom electrode and tungsten (W) refilled cavity layout.

One possible way to reduce the roughness is by re-sputtering a thin film layer of tungsten and then perform a selective and timed etch-back process using hydrogen peroxide 30% H_2O_2 as slow etchant [101]. A negative photo-resist and the photomask layer as shown in Figure 4.5(a) can be used during this process. This process has not been performed in this work that is still under investigation. Tungsten is known to have the tendency to peel-off during the microfabrication process [102]. This problematic behavior of tungsten was observed during this work but the issue

was present in less than ~10% of trenches across the entire 4-inch wafer as shown in Figure 4.7. After characterizing the tungsten (W) layer, the wafer can proceed to the next fabrication step.
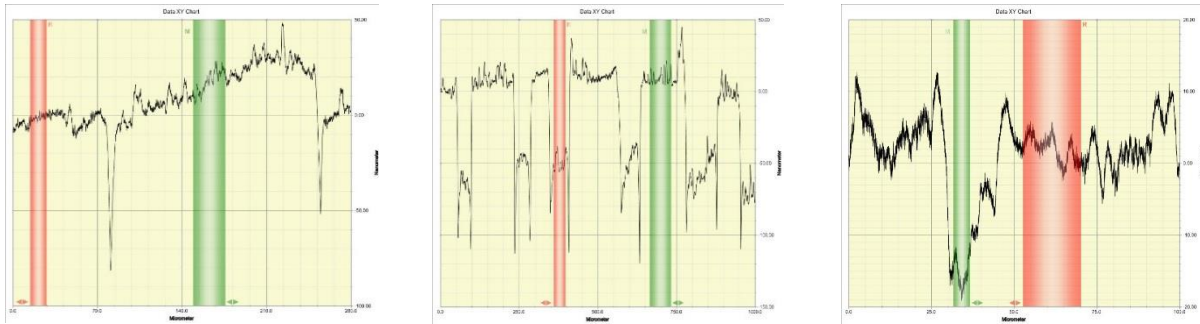
Figure 4.6 – Profilometer images of W/Si roughness.
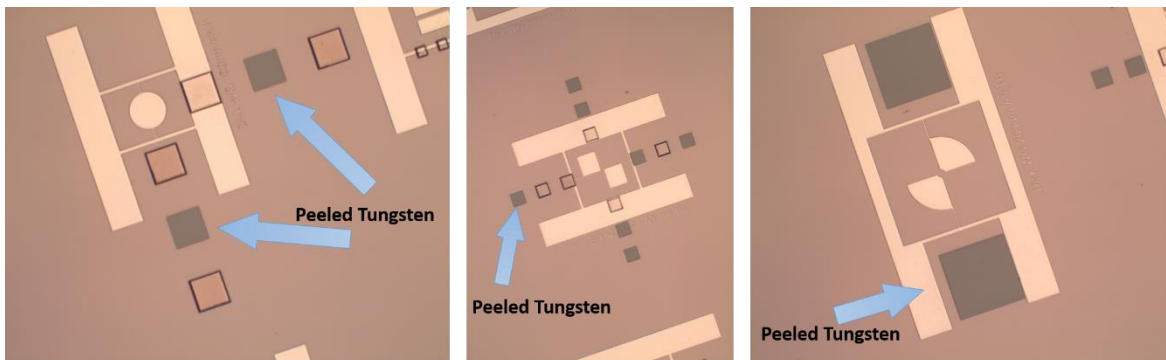
Figure 4.7 – Tungsten peeling issue that has been observed due to the adhesion and other process related stress or material property mismatch.

4.5 TPoS Resonator Process

After the Si/W solid/solid PnCs layer with refilled tungsten (W) is initially defined and processed, the subsequent layers would be the standard TPoS resonator layers. The standard microfabrication process of TPoS resonator consists of a 5 photomask layer process flow. The first four layers are similar to that were illustrated in Figure 3.5, where the ZnO-on-silicon device layer is defined by a reactive ion etching (RIE) process. As shown in Figure 4.8, the RIE process in this work not only etches through the ZnO piezo layer but also pattern the Si device layer subsequently to define the resonator body as shown in Figure 4.9.
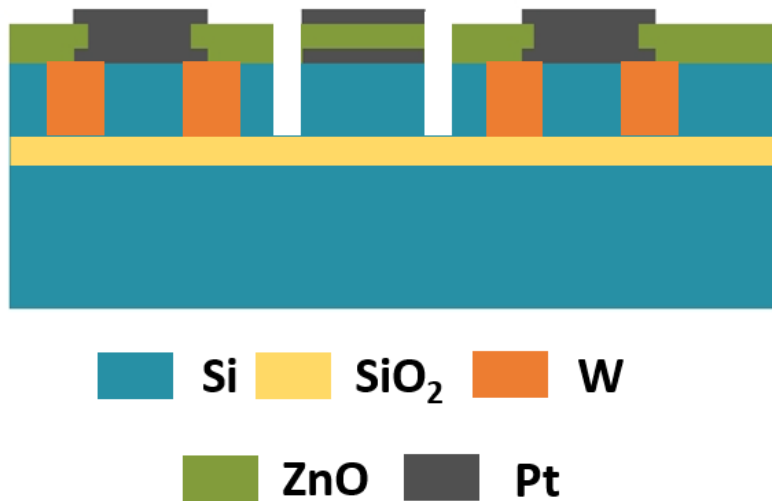
Figure 4.8 – Defined TPoS resonator with PnCs.
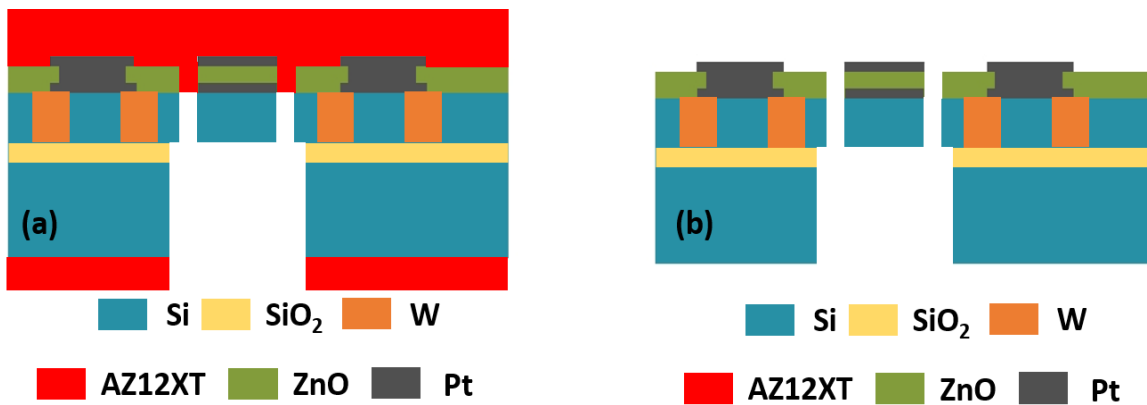
Figure 4.9 – Illustration of the final release process, including (a) backside dry etching; (b) and a mild O_2 plasma ashing to remove photoresist on the front-side of the wafer.

Once TPoS resonators are defined, the next step in the process would be to release and suspend the devices. A back side lithography etch was applied while covering the top devices with a thick photoresist (AZ12XT) layer to protect them. DRIE HAR Bosch process can etch through Si as well as the buried oxide across the whole wafer as can be seen in Figure 4.9. After etching the wafer from the back, a low power oxygen plasma was applied on the top of the wafer to remove the photo-resist using DRIE, which is also known as oxygen ashing process.

4.6 Material Characterization

During microfabrication processes, newly deposited materials, especially those processed in vacuum systems where different gases are circulated such as sputtering, are usually characterized using metrology equipment. Such studies are extremely important to determine the quality of the thin-film material layers at each microfabrication step. This section mainly focuses on tungsten and zinc oxide characterization due to their major roles in how the devices behave.

4.6.1 Tungsten (W)

Tungsten (W) is known to be the strongest metal/element on the periodic table. It has a melting point of 3410 degree Celsius, density of 19.3 g/cc, highest boiling point at 5930 degree Celsius and it is also known for its high tensile strength. In addition, alternated high and low density materials due to the strong dependence of the acoustic impedance on density are essential in forming PnCs, which makes tungsten the most common material used in solid/solid PnCs implementation. Tungsten is almost impossible to deposit using thermal evaporation due to its high melting point, therefore magnetron sputtering and e-beam evaporation are the typical methods used in microfabrication. In this work, Tungsten was sputtered using a DC power source at 100W. Tungsten oxidizes at temperatures between 20-500 degrees Celsius forming different types of oxides such as WO_2 and WO_3[103]. Tungsten oxidation occurs readily when water vapor is present or at high humidity conditions. In order to corroborate that the oxidation layer of W was minimized or avoided, the layer has been studied under energy dispersive x-ray spectroscope (EDS) analysis as shown in Figure 4.10. As shown, the EDS spectrum indicates that the oxygen peak is very minimal and almost nonexistence as compared to typical tungsten oxides found in literature. [103-104].
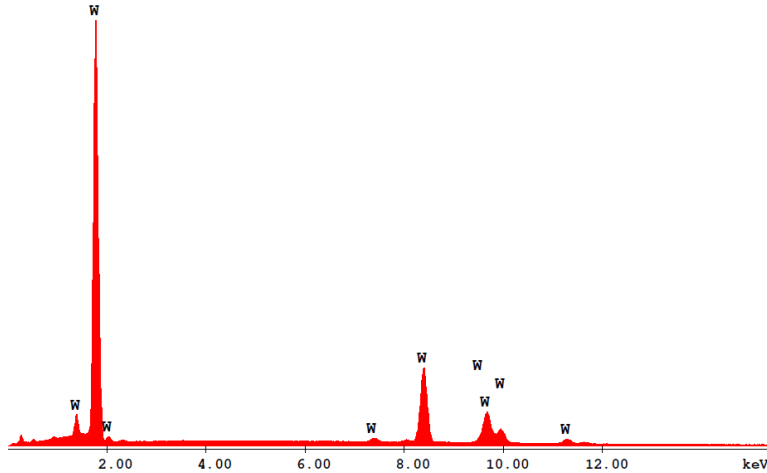
Figure 4.10 – EDS for W layer.

One of the problems that was noticed in the microfabrication of the tungsten is surface cracking. This problem was only observed when depositing tungsten layers thicker than 1um. The tungsten cracking often occurs on top of the photo-resist, before performing the lift-off, while the tungsten on Si did not show such an issue. Figure 4.11 shows a microscopic picture of the tungsten cracking on top of the photoresist covered area. This could be ascribed to the limited temperature stability of the photoresist polymer that has been used.
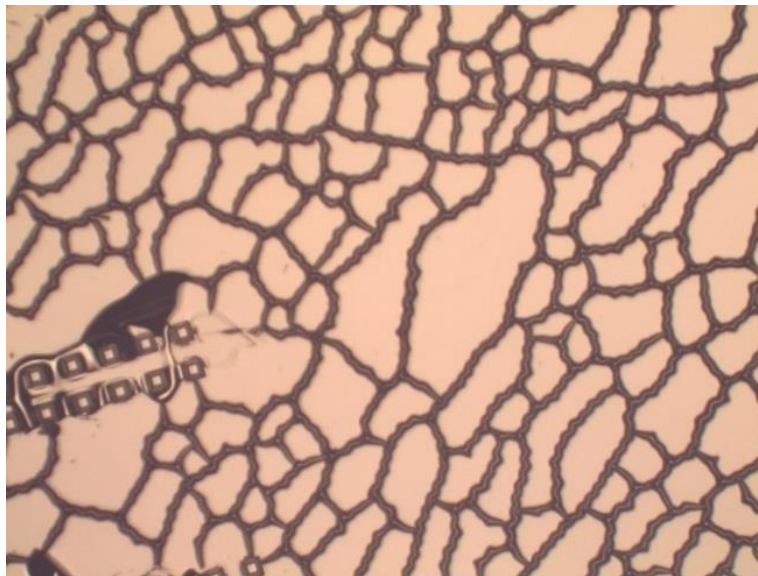
Figure 4.11 – Tungsten cracking.

4.6.2 Zinc Oxide (ZnO)

ZnO is one of II-IV semiconductor materials. ZnO properties can suit for variety of device applications in today's technology such as photocatalytic applications, biomedical applications, etc. Zinc oxide (ZnO) and aluminum nitride (AlN) are the most commonly used piezoelectric materials in MEMS devices. They are both materials compatible with CMOS processing unlike Lead Zirconate Titanate (PZT). While AlN excels in density and acoustic velocity, ZnO is superior to AlN in terms of transverse piezoelectric coefficient d_{31} by offering more than double of its value [105-106]. In this work, ZnO was chosen as the preferred piezoelectric material due to its excellent performance in addition to the fact that it can be defined using a fluorine based reactive ion etching (RIE) process unlike aluminum nitride [106]. In order to obtain high quality ZnO thin film, it is extremely important to study and characterize the deposited thin film to reach the optimal transverse piezoelectric coefficient (d_{31}). The ZnO is deposited using a ceramic target with an 80W of RF power. As it is recommended by all targets suppliers, ceramic targets should be ramped up very carefully to avoid target cracking and deposition failure. Unlike metallic targets, ceramic targets have lower power density of 20 W/square inch in the case of ZnO. In addition to the power density limitation, the ZnO target was noticed to degrade in its electrical properties with time. For instance, ZnO targets that are older than a year were found to have very low volume resistivity on the order of a few Ω.cm making it behaves more like a semiconductive material and ill-suited as a field insulation layer. On the contrary, new targets typically exhibit a volume resistivity more than 10 MΩ.cm, which is several order of magnitude higher.

As mentioned in Chapter 3, the c-002 aligned columnar crystal growth as verified by XRD is one of the highly important parameters in characterizing the ZnO. As shown in Figure 4.12, the observed peak of 2 theta, is located at 34.4 degrees which corresponds to the c-002 axis, which is

an important result for determining piezoelectric behavior response [70]. Meanwhile, Figure 4.13 present the EDS results and the atomic ratio of the oxygen and zinc in the ZnO samples were found to be 53% and 36%, respectively.
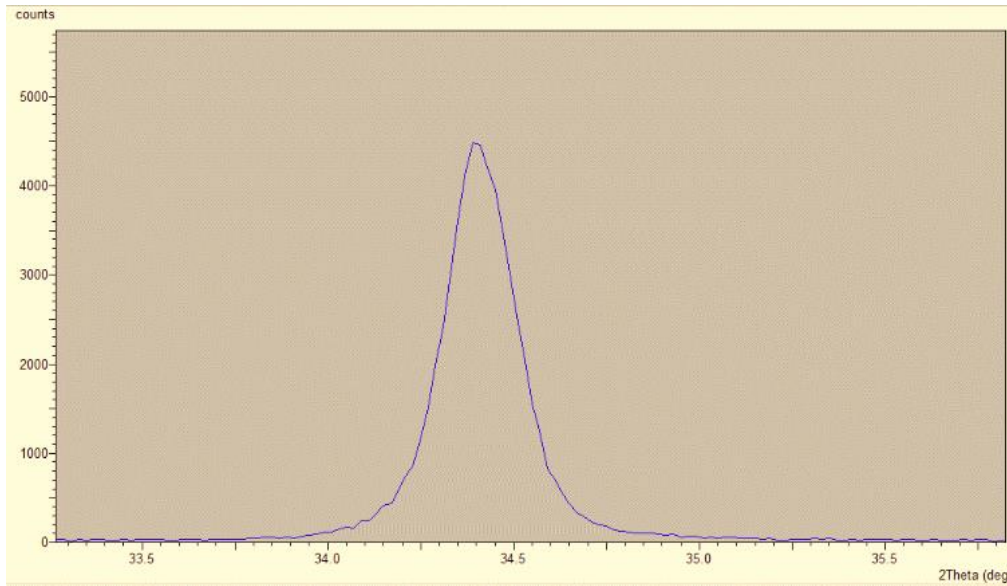
Figure 4.12 – XRD of RF magnetron sputtered ZnO thin film piezoelectric layer.
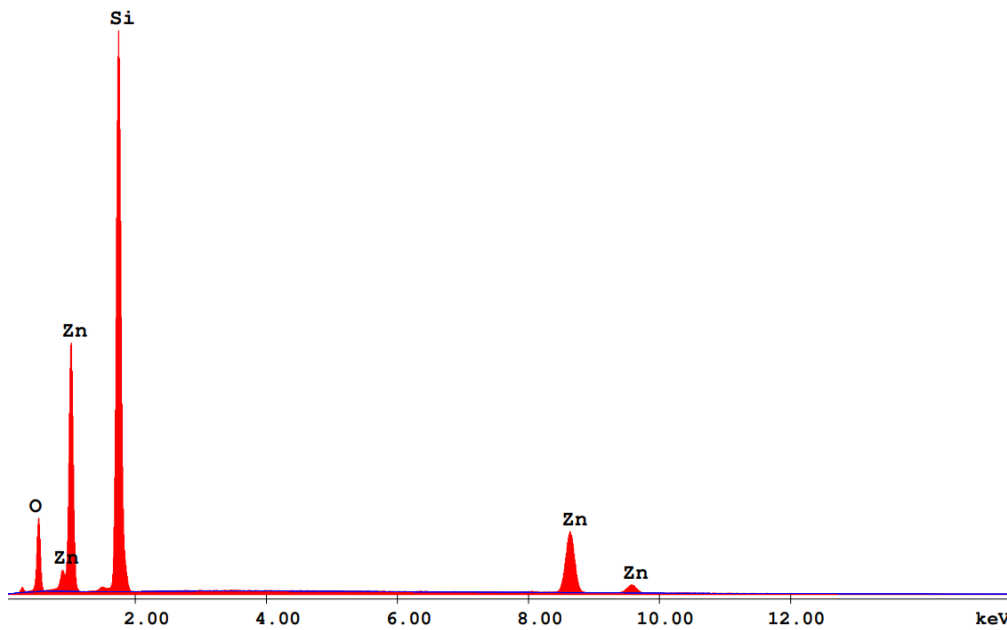
Figure 4.13 – EDS of RF magnetron sputtered ZnO thin film piezoelectric layer.

4.7 SEM Images

All the devices in this work were successfully fabricated and characterized at NREC facility, which also leveraging the AJA Orion 5 UHV sputtering system in IDRB 215 lab. Figure 4.14 shows SEM image of the fabricated devices.
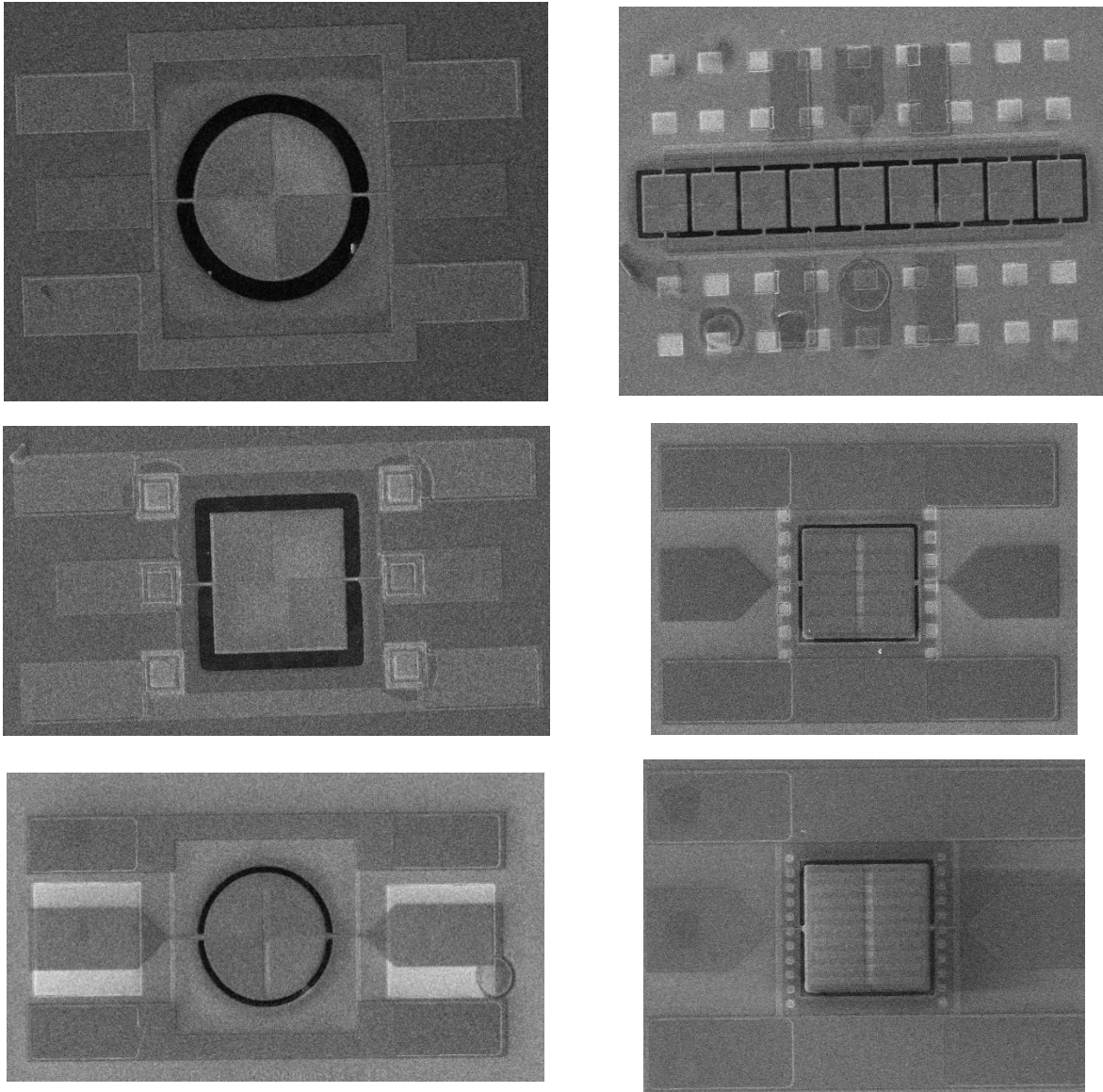
Figure 4.14 – SEM images of fabricated devices.

Chapter 5: Solid/Solid PnCs Effects on Acoustic Field

Today's wireless communication systems and internet of things require high quality factor devices for enabling sensors, filters, oscillators and RF-front-end transceivers. MEMS resonator technology is a key enabler for these wireless communication and sensing systems [68]. In fact, today's 5G communication systems incorporate piezoelectric MEMS resonators widely known as film bulk acoustic resonators (FBAR's) for filter and oscillator implementations [68]. MEMS resonators have been characterized using their figure of merits, which are mainly either products of (Q, k_{eff}) or (Q, f), depending on the application of interest. The quality factor is mostly minimized due to mitigation of the occurrence of the loss mechanisms detailed in Chapter 3. As discussed earlier, the loss mechanisms, especially acoustic loss, in MEMS resonator devices are a bottle neck of resonator application, which degrades their performance. The aim of this work is to reduce the acoustic energy loss of the lateral extensional mode MEMS resonators by implementing PnCs and designing their bandgap to be within the range of the device's operating frequencies. PnCs bandgap is defined as the region, in which no resonance occurs. The employment of PnCs bandgap feature in acoustic MEMS devices allows for significant improvements in the device performance by reflecting the leaked acoustic waves thus retaining the acoustic energy per cycle. In particular, contour mode TPoS resonators have been investigated by many research groups for higher quality factor [25-29]. In this work, the focus is on the strategic design and implementation of solid/solid PnCs by studying their behavior for acoustic wave attenuation within the bandgap regime. Finite Element Method (FEM), based on Comsol Multiphysics software, is used to

quantify the attenuation of the acoustic waves. The acoustic wave reflection caused by PnCs is also observed to occur in the bandgap regime. As such, the quality factor improvement of contour mode TPoS resonators is expected to occur within the bandgap regime. The measured electrical characteristics of the devices have been studied and investigated using BVD model to observe the effect of PnCs on the electrical, mechanical and acoustic behavior of the fabricated devices.

5.1 PnCs BandGap Transmission Study

The amplitude of acoustic waves propagating at a frequency within the phononic bandgap is attenuated greatly due to the nature of PnCs, where no phonons exist within this bandgap region. The bandgap is computed using the Brillouin zone construction by analyzing a single crystal of PnCs and applying the methods discussed in Chapter 2. The solid/solid PnCs study in this work is conducted by quantifying the magnitude of the acoustic wave rejection of a single crystal. Starting with Comsol Multiphysics FEM simulations, the bandgap analysis can be performed by applying the Bloch conditions to the unit cell at the crystal cell periodicity boundary areas as can be seen in Figure 5.1. This allows the assumption of an infinite number of repetitions to the unit cell to perform the subsequent mathematical calculations. This study of the PnCs structure evaluates the eigen-frequencies at each Bloch wave vector within the single crystal. Eq. 2.10 is mathematical equation that governs the periodic condition, which was applied to the phononic crystal structure. The behavior of the PnCs can be predicted by looking at the band diagram. Figure 5.1 shows the wave propagation characteristics of PnCs with regards to its band diagram.

The acoustic spectrum of the forward transmission was evaluated using frequency domain analysis to visualize the PnC mechanism and how it interrupts the transmitted acoustic waves. Pressure is applied at the excitation port, which causes the acoustic wave to travel through the medium, which is silicon in this case. Then, the total displacement is being measured at the output

port with respect to the displacement at the excitation port. The forward transmission is evaluated using the following expression [107]:

$$T_{\text{dB}} = 10 * log\left(\frac{u_{receiver}^2}{u_{transmitter}^2}\right) \tag{5.1}$$
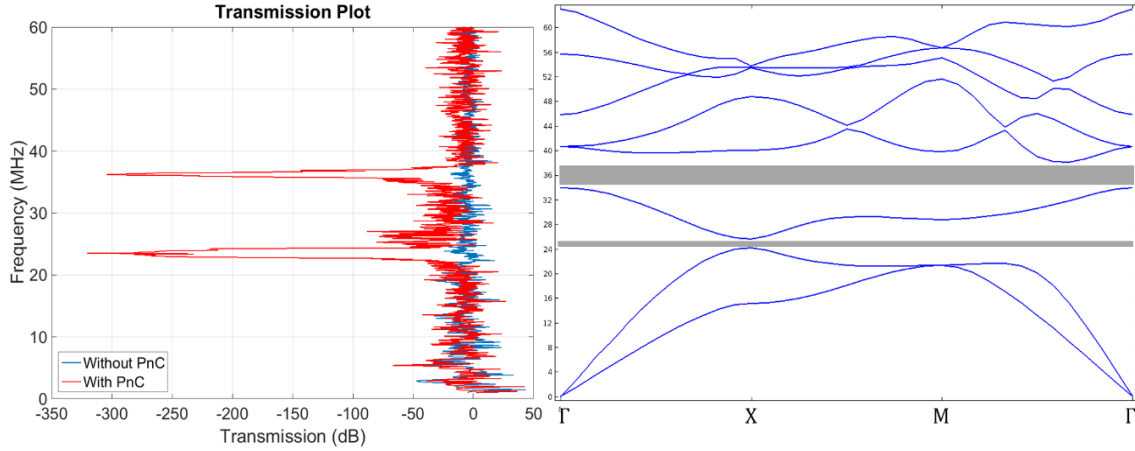
Figure 5.1 – Simulated PnCs transmission attenuation characteristics with respect to bandgap regime.

As can be seen in Figure 5.1, the acoustic wave is diminished within the bandgap regime, which validates the eigen-frequency analysis. It was noticed that the acoustic wave transmission decreases as more crystals are added and interfering with the signals. This behavior was also observed by several research groups using solid/air type PnCs in their works [20-21]. The acoustic attenuation of the phononic crystal was evaluated in this analysis. Each photonic crystal unit cell contributes in the reduction of acoustic signals within the bandgap. The calculated acoustic wave amplitude has dropped by an average of 11 dB per crystal for the frequencies within the bandgap for Si/W PnCs. Additionally, SiO$_2$/W PnCs attenuation is studied in comparison to Si/W. SiO$_2$/W PnCs are popularly used in acoustic attenuation or rejection due to the high acoustic impedance mismatch between tungsten and silicon dioxide. The acoustic impedance mismatch of SiO$_2$/W is higher than that of Si/W by almost 60% as shown in Table 2.2. For comparison, the acoustic

attenuation study is performed on SiO_2/W and the acoustic wave attenuation increases by an average of 18 dB per each crystal within the bandgap regime. Figure 5.2 illustrates the acoustic wave amplitude attenuation in decibel for different quantities of phononic crystals of Si/W PnCs and SiO_2/W PnCs investigated in this work.
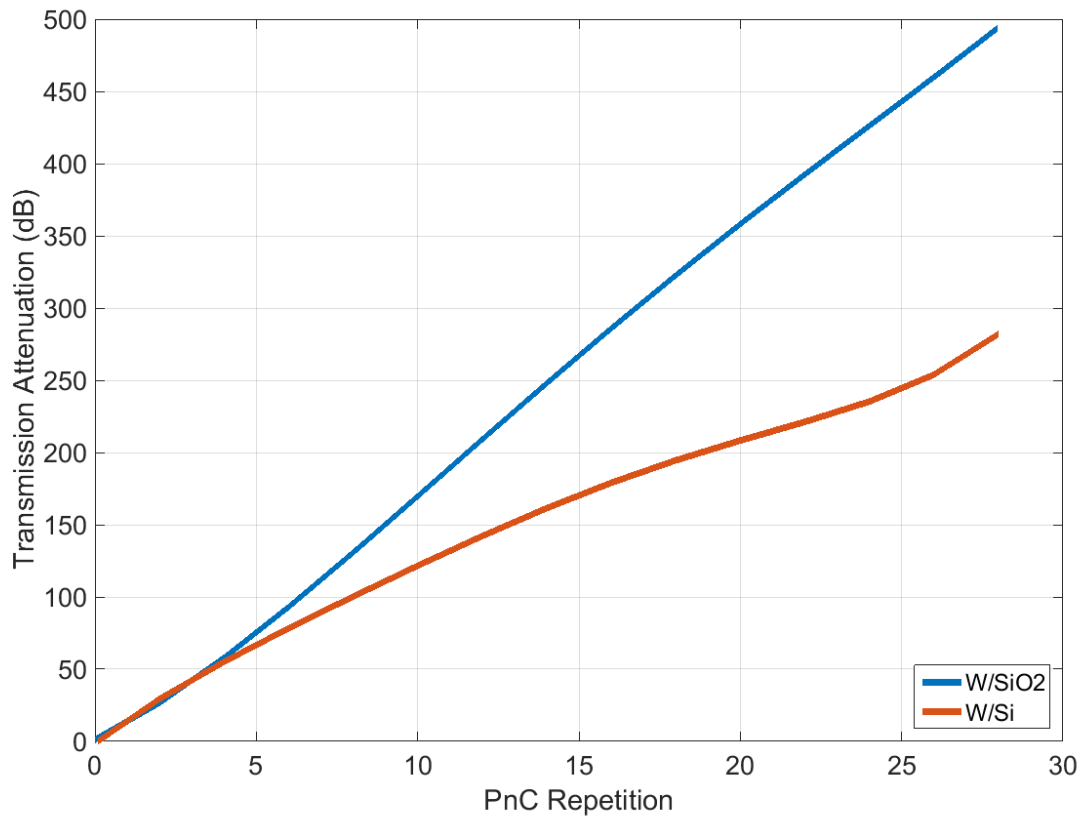
Figure 5.2 – Comparison of W/Si vs W/SiO2 PnCs transmission reduction.

5.2 Anchor Quality Factor

Minimizing anchor loss is essential to improve performance, especially since overcoming loss in MEMS vibrating devices leads to higher quality factor and better figure of merit. Even in capacitively transduced vibrating resonators, where the quality factor tends to be extremely high, anchor loss is still a key performance-limiting factor that needs to be mitigated [64]. Several works have already been developed, especially with a focus on Solid/Air type of PnCs, to overcome the

anchor loss effect in capacitive and piezoelectric microresonators as mentioned earlier [25-29]. Although piezoelectrically transduced MEMS resonators typically exhibit lower quality factor as compared to capacitively transduced counterparts, they still are the dominant devices used in commercial applications. Piezoelectric resonators tend to have very low motional resistance, thus allowing them to be readily impedance matched to RF-front-end circuitry unlike the capacitive devices. Improving best achievable performance of piezoelectric resonators is the main scope of this dissertation work. The acoustic wave leakage that occurs through the supporting tethers during the lateral extensional resonator vibration degrades the resonators' performance. By strategically designing the phononic crystals and their bandgap regime to match with the resonator devices' vibrating resonances, the MEMS resonator devices equipped with PnCs are anticipated to exhibit higher quality factors [25-29,63]. Several strategies other than PnCs have been previously attempted by others to reduce the anchor loss such as positioning the anchors at the nodal locations of the designed resonance mode, quarter wavelength anchor length or its odd multiples, acoustic mirrors, and reshaping of the devices' edges using butterfly, spider-web and frame shapes [72,108-110]. All these strategies have shown noticeable improvements of quality factor indicating great suppression of the acoustic wave leakage through the supporting anchor toward the substrate. The investigation of the anchor designs is generally validated using perfectly matched layer (PML) technique in FEM software such as COMSOL Multiphysics. The applicability of PML is valid to all different types of waves that fall into the similar mathematical wave equations type of partial differential equations as Maxwell's equations. The PML design in this work is implemented to absorb all the outgoing acoustic waves and eliminate the acoustic reflections. The acoustic wave decays exponentially when it travels through the PML regime. Figure 5.3 and Figure 5.4 show a suspended disk resonator fixed at one anchor attached to the substrate via a supporting tether. The

resonator disk radius is set to be 50 μm and its anchor is attached to the substrate that is surrounded by PML regime. The radius of the substrate and the PML is set as twice and 1.35 times of the wavelength (2λ and 1.35λ), respectively. Since the scope of this work is focused on the suppression of the acoustic wave leakage through the supporting tether, other losses such as air damping and material losses are ignored in this study. The quality factor of disk resonator operating at its first lateral contour mode is observed under different PnCs repetition designs as shown in Table 5.1. The quality factor due to anchor related losses can be calculated in FEM COMSOL Multiphysics using the ratio between real and imaginary parts at the disk resonator modal frequency. Q_{anchor} can be expressed as [108].

$$Q_{anchor} = \frac{Re(2*pi*f)}{2*Im(2*pi*f)} \tag{5.2}$$
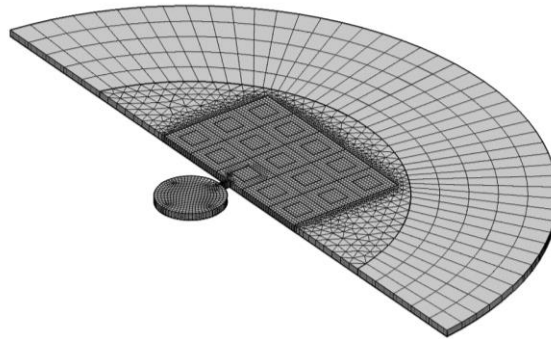
Figure 5.3 – Meshed FEM model of anchor supported disk resonator with an array of PnCs.
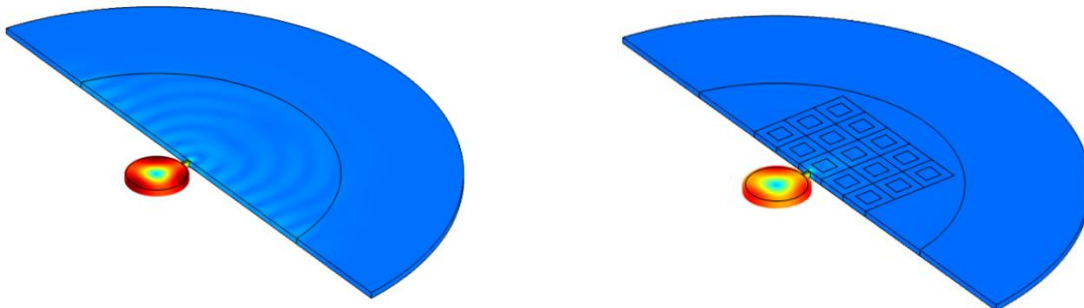
Figure 5.4 – COMSOL simulated acoustic wave reflection from the PnCs.

Table 5.1 – PnCs repetition effects on best achievable quality factor

Design	Quality Factor
No PnCs Implemented	454
One PnCs Repetition	3,454
Two PnCs Repetition	26,514
Three PnCs Repetition	83,770

5.3 RF MEMS Circuits

For an adequate MEMS resonator device characterization, the electrical and mechanical equivalent circuit components can be extracted out of the measrued frequency responses. As reviewed in Chapter 3, mechanical components and electrical components are equivalently related. Although mechanical and acoustic properties describe the actual state of the device, the RF test of electrical freuency charactersic properties are the most commonly used measurements since most applications require these measured devices to be integrated with different integrated circuits such as accelerometers used in airbags for automobiles industry, RF transceivers circuits used in the wireless communication industry, etc [68]. As such, MEMS designs require full understanding of the fundamental electrical circuits to apply the extracted equivlent circuit parameters from MEMS devices in the electrical circuit schematic, especially when coupling with additional electrical components such as amplifiers in oscillator applications and so on. Electrical characterization involves understanding the basics of network theory and measurement techniques necessary to extract the equivalent circuit parameters, the quality factor, the electromechanical coupling, etc.

For most MEMS devices under test (DUT), the electrical setup can be represented as three elements: signal generator or vector network analyer (VNA), DUT and a load. Generally, the main

measurement is the current delivered to the load after passing through the DUT (e.g., resonator) as seen in Figure 5.5.
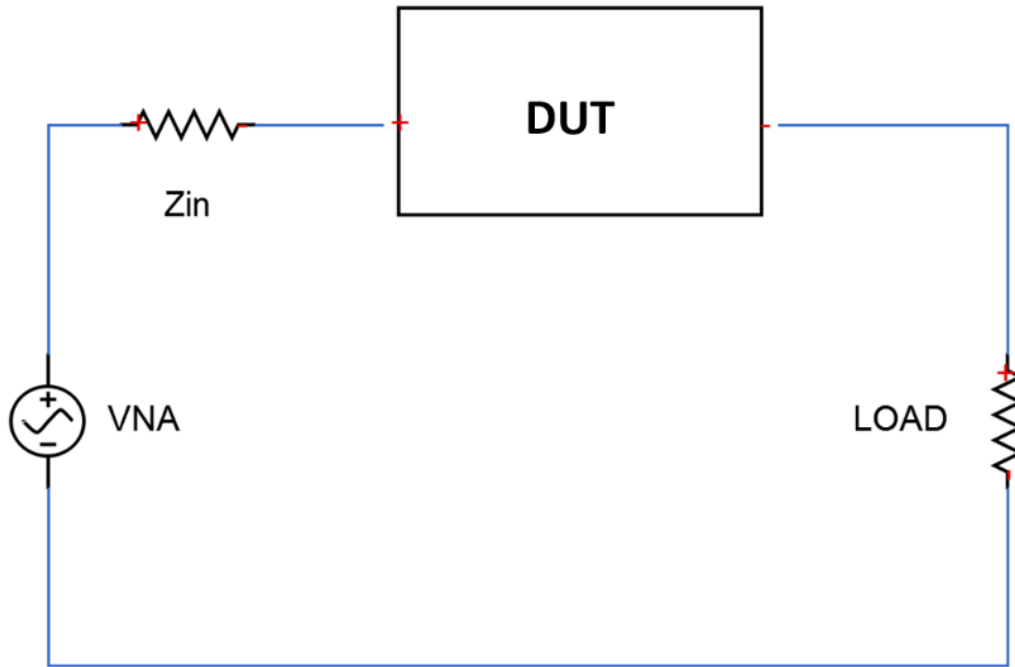
Figure 5.5 – Typical electrical characterization of MEMS DUT devices such as resonators.

Continuity test is also required during microfabrication process to validate the fabricated device to be testable. Therefore, it is crucial to perform the open-short test for the electrode pads of the two ports connected to the devices. This measurement is critical to confirm the state of the devices and reassure that they are successfully fabricated and the ports were not disconnected during the process.

In RF microwave engineering circuits, scattering parameters are the most suitable method to analyze the electrical circuit at high frequency ranges, where signal power waves and energy of the RF system are computed rather than voltages and currents. In essence, S-parameters solve for the transmitted and reflected waves at each port of the RF system. Most MEMS resonators can be represented as two-port system network. Figure 5.6 presents a two-port system S-parameters.

Figure 5.6 – S-parameter for two port RF MEMS network.

The matrix of the system scattering parameters can be written as

$$\begin{bmatrix} b_1 \\ b_2 \end{bmatrix} = \begin{bmatrix} S_{11} & S_{12} \\ S_{21} & S_{22} \end{bmatrix} \begin{bmatrix} a_1 \\ a_2 \end{bmatrix} \tag{5.3}$$

The S-parameters can be solved by terminating each port of the system with a matched load (setting $a_{1,2}=0$)

$$\left| \begin{array}{ll} S_{11} = \dfrac{b_1}{a_1} & S_{12} = \dfrac{b_1}{a_2} \\ S_{21} = \dfrac{b_2}{a_1} & S_{22} = \dfrac{b_2}{a_2} \end{array} \right| \tag{5.4}$$

where, S_{11} and S_{21} are the reflection coefficient and the transmission coefficient, respectively. They can be determined when port 2 is terminated with a matched load ($a_2=0$). Similarly, for S_{22} and S_{12}, their values can be determined, when port 1 is terminated with a matched load ($a_1=0$).

5.4 Quality Factor Extraction

For MEMS resonators, performance in sensing applications, communication applications, etc. is often strongly dependent on its quality factor. Several approaches to extract the Q factor have been used, however, the most commonly used method for Q extraction is the 3-dB bandwidth. Simply, the quality factor can be defined as the peak of the resonance frequency at its lowest insertion loss divided by the difference of the two frequencies that have 3dB offset on each side the resonance peak. The equation of the Q calculation can be expressed as [152]:

$$Q = \frac{f}{BW_{3dB}} \qquad (5.5)$$

Quality factor has many dependent factors as mentioned in Chapter 2. Insertion loss also has a dependency on the quality factor as shown in Equation 5.6

$$IL(dB) = 20 * \log\left(\frac{1}{1 + \frac{0.75 * \pi^2}{k_{eff}^2 Q}}\right) \qquad (5.6)$$

The equation shows the relation between Q and insertion loss, and indicates that higher quality factor is essential for achieving lower insertion loss. Figure 5.7 shows that a resonator device could reach to perfect performance given optimized materials are provided.

The MEMS resonator device frequency responses could also be enhanced by improving the electromechanical coupling coefficient, which ultimately would lead to a better performance. In MEMS transducers, electromechanical coupling coefficient (k_{eff}) is the efficiency for converting the energy between electrical to mechanical domains.
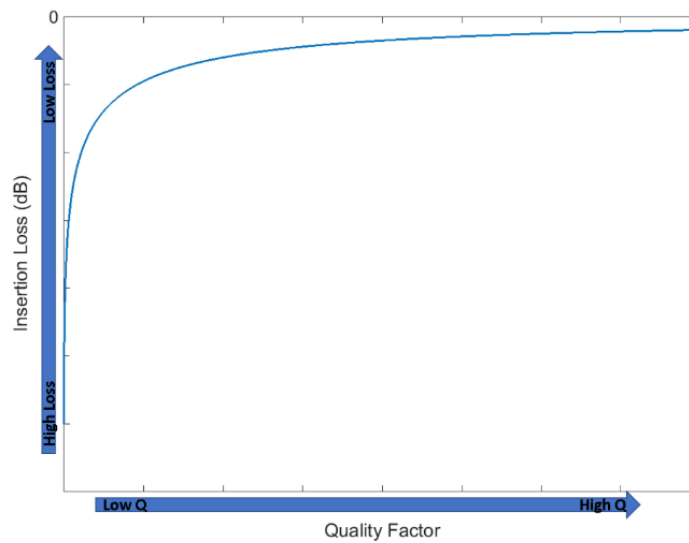
Figure 5.7 – Insertion loss dependency of quality factor in MEMS devices.

The square value of electromechanical coupling coefficient can be calculated as the ratio of mechanical energy E_M to the electrical energy E_E and can be measured experimentally using the series and parallel resonances based on measured frequency response [68].

$$k_{eff}^2 = E_M * (E_E + E_M)^{-1} = \frac{\pi^2(f_p - f_s)}{4f_p} \tag{5.3}$$

The fabricated devices, with and without PnCs, have been measured in ambient air environment. The response of device equipped with PnCS have exhibited enhanced Q factor by about 7 times. Figure 5.8 presents the measured frequency responses, which shows noticeable Q enhancement by ~ 7 times as compared to the normal response of a device without PnCs, whereas other responses shown in Fig. 5.8 (c) shows no Q enhancement effects compared to the normal response indicating no acoustic reflection, when it operates outside the phononic crystal bandgap frequency range.

(a)
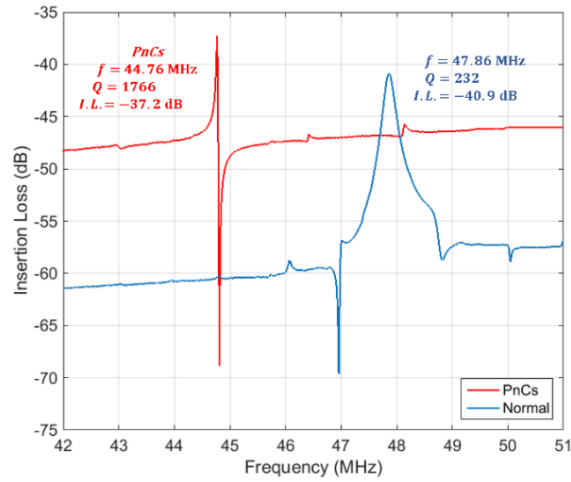
(b)
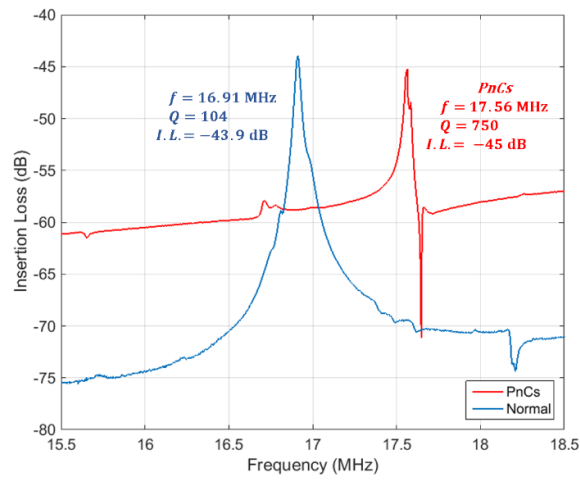
(c)
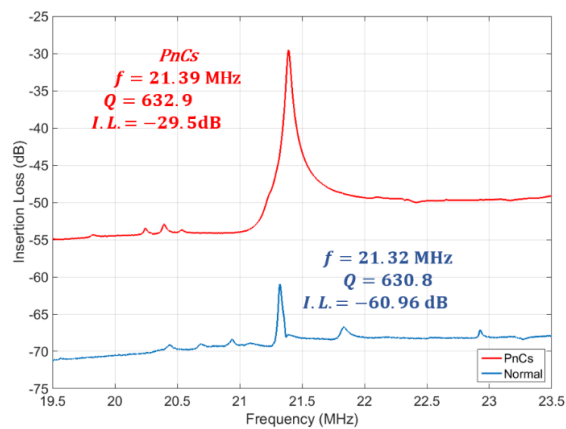
Figure 5.8 – Measured forward transmission responses of fabricated devices with and without strategically designed PnCs, which enhance the Q factor when operating in the phononic bandgap.

Chapter 6: Conclusions and Future Work

6.1 Summary of the Contribution and Ongoing Work

The original work in this dissertation has focused on the strategic design and development of thin-film piezoelectric-on-silicon (TPoS) resonators using a single crystalline silicon wafer rather than a silicon-on-insulator (SOI) wafer. In addition, an optimized fabrication process to produce cost effective TPoS resonators as compared to previous device counterparts typically microfabricated by expensive SOI technology. The lateral extensional mode TPoS resonators have been fabricated successfully using the modified process. The demonstrated fabrication process utilized a modified version of the traditional single crystal reactive etching and metallization (SCREAM) process, which has been widely used in capacitive MEMS devices such as accelerometers and gyroscopes. As a unique MEMS release technique developed in this work to fabricate TPoS resonators, this process supports the batch fabrication of resonators with varying thicknesses ranging from 0.1 micrometer upto 50 micrometers on the same single crystal silicon wafer. The TPoS devices fabricated using this modified technique have demonstrated loaded Q factor higher than 1,000 and motional impedances as low as a few hundred ohms.

A thorough investigation of one and two dimensional solid/solid PnC is introduced in this dissertation. To the author's knowledge, this work pioneered the implementation of such types of solid/solid PnCs in suspended MEMS bulk acoustic wave (BAW) resonator devices, particularly TPoS resonators. The theoretical analysis of the solid/solid PnCs was introduced and has been validated through Comsol Multiphysics finite element method (FEM) simulations. The alternated materials of the PnCs were selected in such way that they would not introduce additional

complexity in microfabrication and satisfy the conditions of blocking the acoustic wave leakage from the supporting anchors of the vibrating TPoS resonator devices. Different designs of high RF frequency vibrating resonator devices were also investigated in this work.

The solid/solid PnCs microfabrication uniquely introduced in this work is defined by utilizing two sequential steps in a single lithography process. In addition, a 2 μm thick layer of tungsten employed for solid/solid PnCs implementation showed complications during the film deposition such as surface cracking. It is possible to avoid cracking by using e-beam evaporation for tungsten deposition but this process was not studied in this work due to the difficulty of maintaining the extremely high voltage and current necessary to evaporate tungsten for a prolonged period of time, which could possibly result in danger to the user. In addition, the lift-off process will pose extra complexity in the e-beam evaporation because the high temperature of the evaporated tungsten on the photoresist, which could potentially bake and harden the photoresist. The material characteristics of the chosen TPoS resonator structure layers are investigated using metrology equipment such as X-Ray diffraction and EDS.

FEM analysis by Comsol Multiphysics is used in this work to study the acoustic transmission in plain structural material, which is then interrupted by PnCs, to study the amount of signal-to-noise ratio change due to the incorporation of PnCs. PnCs' signal reduction or signal blocking characteristics were compared and matched to the bandgap study. Then the effect of the PnCs embedded the disk resonators supporting anchors were studied. The quality factor of the resonators equipped with newly designed solid/solid PnCs has been increased by a factor of ~10. This indicates that the acoustic leakage through the resonator supporting anchors has been significantly reduced due to employment of newly designed PnCs that has led to higher Q factors.

6.2 Future Work

The removal of the thin film ALD layer in the modified TPoS fabrication process using the single crystalline silicon wafer can further improve the results, but that would require HF wet etch. One way to utilize that is by replacing the ZnO thin film with another piezoelectric material that doesn't get attacked by HF etchant. The most common piezoelectric material in MEMS devices that meets this requirement is RF sputtered AlN. The lack of a chlorine dry etch system at the USF NREC facility, which is needed for AlN anisotropic etch, prevents this AlN work from continuing. Availability of such systems in the future at USF NREC or collaboration with outside labs would allow this investigation to progress, which is anticipated to lead to improved performance.

The results from this work have demonstrated the feasibility of implementing PnCs designs to incorporate into the current MEMS resonator technology. This implementation was proven to not only be compatible with the microfabrication process but also could potentially improve future MEMS resonator performance significantly by taking advantage of low loss materials such as Si and diamond, which has been widely used electrostatically transduced resonator technology. By implementing solid/solid PnCs into piezoelectrically transduced, lateral extensional mode MEMS resonators, both the high electromechanical coupling (low motional impedance) and low acoustic energy loss (high-Q) can be achieved. By strategically designing the PnCs in the manner as shown in Figure 6.1, higher Q resonators with higher signal or electromechanical coupling coefficient can be achieved. Electrode patterns can be further strategically designed to match the vibration modes based on the FEM simulation model developed in this work. Also, electrode material needs to be explored along with compatible fabrication processes. Meanwhile, the electrode thickness needs to be optimized for reducing the conductor losses and acoustic energy dissipations.
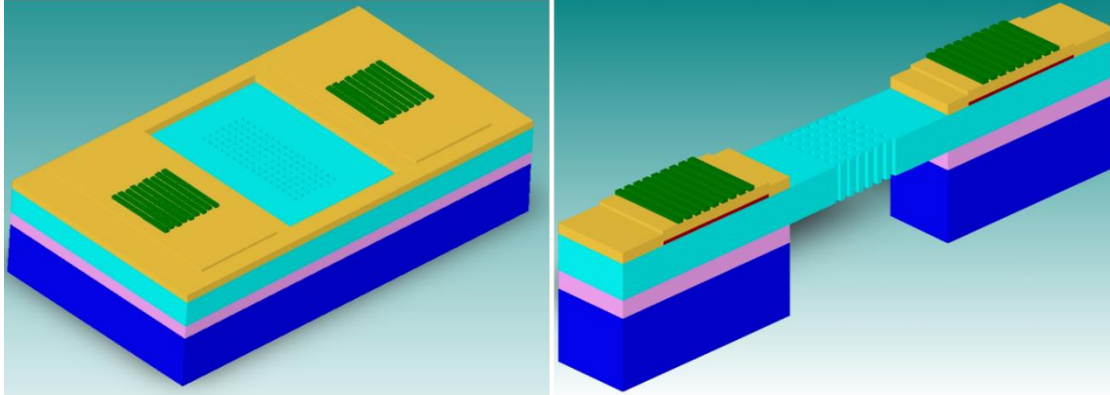
Figure 6.1 – Future model of thin-film piezoelectric resonators equipped with solid/solid PnCs for further improving the overall device performance.

Using the fabrication process as seen in Fig. 6.1, different designs can be implemented to observe the acoustic energy loss reduction by maximizing the effects of the PnCs. Besides silicon, other high Q acoustic materials, especially diamond, have not been investigated thoroughly in MEMS resonator and PnCs applications. Implementing different materials could possibly increase device performance as long as they meet the requirements discussed in this dissertation.

The microfabrication of solid/solid PnCs in released TPoS resonators needs to be optimized to avoid the complications encountered in this work such as the cracking and peeling of tungsten, and to achieve a better lateral/transversal piezoelectric coefficient d31. Additionally the work in this dissertation can be further developed by studying the effects of resonator stacked layers against temperature at the resonances. This effect can be characterized by the temperature coefficient of resonance frequency and it depends on material properties and geometry. The dependency of the Young's Modulus (E) is the dominant factor in the material properties. The geometric dependence is represented by the thermal expansion coefficient (α) that is neglected due to smaller influence. The overall equation of the temperature coefficient of resonance frequency can be written as:

$$TC_f = \sqrt{\left(\sum_n \frac{(1 + TC_{E_n})E_n t_n}{E_n t_n}\right) - 1}$$

(6.1)

Unfortunately, not all the strategically designed devices in this work have been measured successfully due to several complications during microfabrication. During the future works, the microfabrication process needs to be optimized in such a way that tungsten doesn't crack on its surface or peel off during process. In addition, the in-house zinc oxide needs to be optimized to reach its maximum quality and highest achievable piezoelectric coefficient. Overcoming these obstacles would allow several studies of PnCs including crystal repetition, anchor alignment, and so on. Nevertheless, the research work in this dissertation shows a great promise for solid/solid PnCs designs, which shall be further investigated in the future works.

References

[1] W. E. Newell, "Face-mounted piezoelectric resonators," Proceedings of IEEE, 53 (6), pp.575-581, 1965

[2] Yablonovitch, Eli, "Inhibited Spontaneous Emission in Solid-State Physics and Electronics", Phys. Rev. Lett., vol. 58, pp. 2059—2062, 1987

[3] Kushwaha, M. S. and Halevi, P. and Dobrzynski, L. and Djafari-Rouhani, B, "Acoustic band structure of periodic elastic composites", Phys. Rev. Lett., vol. 71, pp. 2022—2025, 1993

[4] R. Martinez-Sala, J. Sancho, J. V. Sanchez, V. Gomez, J. Llinares, and F. Meseguer, "Sound attenuation by sculpture," Nature, vol. 378, p. 241, 1995

[5] Kushwaha,Manvir S., "Stop-bands for periodic metallic rods: Sculptures that can filter the noise", Appl. Phys. Lett., vol. 70, pp. 3218—3220, 1997

[6] Montero de Espinosa, F. R. and Jimenez, E. and Torres, M., "Ultrasonic Band Gap in a Periodic Two-Dimensional Composite", Phys. Rev. Lett., vol. 80, pp. 1208—1211, 1998

[7] Zhengyou Liu, Xixiang Zhang, Yiwei Mao, Y. Y. Zhu, Zhiyu Yang, C. T. Chan, Ping Sheng*, "Locally Resonant Sonic Materials," Science, vol. 289, pp. 1734-1736, 2000

[8] Wu,Tsung-Tsong, Wu,Liang-Chen, Huang,Zi-Gui "Frequency band-gap measurement of two-dimensional air/silicon phononic crystals using layered slanted finger interdigital transducers", Journal of Applied Physics, vol. 97, pp., 2005

[9] T. Miyashita, "Sonic crystals and sonic wave-guides," Meas. Sci. Technol. 16, 47–63, 2005

[10] M. M. Sigalas, García,N., "Theoretical study of three dimensional elastic band gaps with the finite-difference time-domain method," J. Appl. Phys. Vol. 87, pp. 3122-3125, 2000

[11] Kee C-S, Kim J-E, Park H Y, Chang K J and Lim H, "Essential role of impedance in the formation of acoustic band gaps," J. Appl. Phys. Vol.87, pp. 1593-1596, 2000

[12] Kafesaki M, and Economou E N, "Multiple-scattering theory for threedimensional periodic acoustic composites,"Phys. Rev. B., vol. 60, pp. 11993-12001, 1999

[13] Su J-C and Wu T-T, "Bleustein-Gulyaev-Shimizu surface acoustic waves in two-dimensional piezoelectric phononic crystals," IEEE Trans. Ultrason. Ferroelectr. Freq. Control, vol. 53, pp. 1169-1176, 2006

[14] Vasseur J O, Deymier P A, Chenni B, Djafari-Rouhani B, Dobrzynski L and Prevost D, "Experimental and theoretical evidence for the existence of absolute acoustic band gaps in two-dimensional solid phononic crystals," Phys. Rev. Lett., vol. 86, pp. 3012-3015, 2001

[15] Hsiao F, Khelif A, Moubchir H, Choujaa A, Chen C and Laude, "Complete band gaps and deaf bands of triangular and honeycomb water-steel phononic crystals," J. Appl. Phys., vol. 101, pp. 044903, 2007

[16] Yang S, Page J H, Liu Z, Cowan M L, Chan C T and Sheng P, "Ultrasound tunneling through 3D phononic crystals," Phy. Rev. Lett., vol. 88, pp. 104301, 2002

[17] Dhar. Lisa, Rogers. John A., "High frequency one-dimensional phononic crystal characterized with a picosecond transient grating photoacoustic technique," Phy. Rev. Lett., vol. 77, pp. 1402-1404, 2000

[18] M. Ziaei-Moayyed, M. F. Su, C. Reinke, I. F. El-Kady and R. H. Olsson, "Silicon carbide phononic crystal cavities for micromechanical resonators," 2011 IEEE 24th International Conference on Micro Electro Mechanical Systems, Cancun, 2011, pp. 1377-1381

[19] Hemon S., Akjouj A., Soltani A., Pennec Y., El Hassouani Y., Talbi A., Mortet V., Djafari-Rouhani B., "Hypersonic band gap in an AlN-TiN bilayer phononic crystal slab," Phy. Rev. Lett., vol. 104, pp. 063101, 2014

[20] S. Benchabane, A. Khelif, J. Y. Rauch, L. Robert, V. Laude, "Lithium niobate phononic crystal for surface acoustic waves," Proc. SPIE 6128, Photonic Crystal Materials and Devices IV, 61281A (1 March 2006)

[21] Su M. F., Olsson R. H., Leseman Z. C., El-Kady I., " Realization of a phononic crystal operating at gigahertz frequencies," Phy. Rev. Lett., vol. 96, pp. 05311, 2010

[22] R. H. Olsson , J. G. Fleming, M. R. Tuck, "Contour mode resonators with acoustic reflectors," US patent 7385334 B1, 2008

[23] W. Wang, D. Weinstei, "Unreleased MEMS resonator and method of forming same," U.S. Patent 20130033338, 2012

[24] R. Marathe, B. Bahr, W. Wang, Z. Mahmood, L. Daniel and D. Weinstein, "Resonant Body Transistors in IBM's 32 nm SOI CMOS Technology," in Journal of Microelectromechanical Systems, vol. 23, no. 3, pp. 636-650, June 2014

[25] Xu Dehui, Wu Guoqiang, Xiong Bin, Wang Yuelin,"Phononic crystal strip based anchors for reducing anchor loss of micromechanical resonators", Journal of Applied Physics, vol. 115, pp. 024503, 2014

[26] C. Lin, J. Hsu, D. G. Senesky and A. P. Pisano, "Anchor loss reduction in ALN Lamb wave resonators using phononic crystal strip tethers," 2014 IEEE International Frequency Control Symposium (FCS), Taipei, 2014, pp. 1-5

[27] P. Qin, H. Zhu, J. E. -. Lee and Q. Xue, "Phase Noise Reduction in a VHF MEMS-CMOS Oscillator Using Phononic Crystals," in IEEE Journal of the Electron Devices Society, vol. 4, no. 3, pp. 149-154, May 2016

[28] M. W. U. Siddiqi and J. E. -. Lee, "AlN-on-Si MEMS resonator bounded by wide acoustic bandgap two-dimensional phononic crystal anchors," 2018 IEEE Micro Electro Mechanical Systems (MEMS), Belfast, 2018, pp. 727-730

[29] Wang, S., L. Popa and D. Weinstein. "GAN MEMS RESONATOR USING A FOLDED PHONONIC CRYSTAL STRUCTURE." (2014)

[30] M. Maldovan, "Sound and heat revolutions in phononics," Nature, vol. 503, pp. 209-17, Nov 14 2013

[31] Patrick E. Hopkins, Charles M. Reinke, Mehmet F. Su, Roy H. Olsson, Eric A. Shaner, Zayd C. Leseman, Justin R. Serrano, Leslie M. Phinney, and Ihab El-Kady, "Reduction in the Thermal Conductivity of Single Crystalline Silicon by Phononic Crystal Patterning" Nano Letters, 2011, vol. 11, pp. 107-112

[32] R. H. Olsson et al., "Ultra high frequency (UHF) phononic crystal devices operating in mobile communication bands," 2009 IEEE International Ultrasonics Symposium, Rome, 2009, pp. 1150-1153

[33] R. H. Olsson, J. G. Fleming, I. F. El-Kady, M. R. Tuck and F. B. McCormick, "Micromachined Bulk Wave Acoustic Bandgap Devices," TRANSDUCERS 2007 - 2007 International Solid-State Sensors, Actuators and Microsystems Conference, Lyon, 2007, pp. 317-321

[34] Zhu, J., Christensen, J., Jung, J. et al. A holey-structured metamaterial for acoustic deep-subwavelength imaging. Nature Phys 7, 52–55 (2011)

[35] R. Lanz, M. -A. Dubois and P. Muralt, "Solidly mounted BAW filters for the 6 to 8 GHz range based on AlN thin films," 2001 IEEE Ultrasonics Symposium. Proceedings. An International Symposium (Cat. No.01CH37263), Atlanta, GA, USA, 2001, pp. 843-846 vol.1

[36] Roy H. Olsson, Ihab F. El-Kady, Mehmet F. Su, Melanie R. Tuck, James G. Fleming, "Microfabricated VHF acoustic crystals and waveguides," Sensors and Actuators A: Physical, Vol. 145–146, pp. 87-93, 2008

[37] Khelif, A. and Choujaa, A. and Djafari-Rouhani, B. and Wilm, M. and Ballandras, S. and Laude, V., "Trapping and guiding of acoustic waves by defect modes in a full-band-gap ultrasonic crystal" Phys. Rev. B., vol. 21, pp. 214301, 2003

[38] R Lucklum and J Li, " Phononic crystals for liquid sensor applications," Meas. Sci. Technol. 20, 2009

[39] El-Kady, Ihab F, Olsson, Roy H, Hopkins, Patrick, Reinke, Charles, and Kim, Bongsang. Synthetic thermoelectric materials comprising phononic crystals. United States: N. p., 2013

[40] Lv Hangyuan, Tian Xiaoyong, Wang Michael Yu, Li Dichen, "Vibration energy harvesting using a phononic crystal with point defect states" Applied Physics Letters, vol. 102, pp. 034103

[41] Vasseur J O, Hladky-Hennion A-C, Djafari-Rouhani B, Duval F, Dubus B, Pennec Y and Deymier P A, "Waveguiding in two-dimensional piezoelectric phononic crystal plates," J. Appl. Phys., vol. 101, pp. 114904, 2007

[42] Khelif A, Choujaa A, Benchabane S, Djafari-Rouhani B and Laude V, "Guiding and bending acoustic waves in highly confined phononic crystal waveguides," Appl. Phys. Lett., vol. 84, pp. 4400-4402, 2004

[43] Yang S, Page J H, Liu Z, Cowan M L Chan C T and Sheng P, "Focusing of sound in a 3D phononic crystal," Phys. Rev. Lett., Vol. 93, pp. 024301, 2004

[44] Zhang X, and Liu Z, "Negative refraction of acoustic waves in two-dimensional phononic crystals," Appl. Phys. Lett., vol. 85, pp. 341-343, 2004

[45] Ke M, Liu Z, Qiu C, Wang W, Shi J, Wen W and Sheng P, "Negative-refraction imaging with two-dimensional phononic crystals," Phys. Rev. B, vol. 72, pp. 064306, 2005

[46] S. Villa-Arango, R. Torres, P.A. Kyriacou, R. Lucklum, "Fully-disposable multilayered phononic crystal liquid sensor with symmetry reduction and a resonant cavity," Measurement, Vol. 102, pp. 20-25, 2017

[47] I. El-Kady, R. H. Olsson III, P. E. Hopkins, Z. C. Leseman, D. F. Goettler, B. Kim, C. M. Reinke, and M. F. Su, Phonon Manipulation with Phononic Crystals, Progress report SAND2012-0127 (Sandia National Laboratories, California, CA, 2012)

[48] Choon-Su Park, Yong Chang Shin, Soo-Ho Jo, Heonjun Yoon, Wonjae Choi, Byeng D. Youn, Miso Kim, "Two-dimensional octagonal phononic crystals for highly dense piezoelectric energy harvesting," Nano Energy, vol. 57, pp. 327-337, 2019

[49] Page,J. H., "Focusing of ultrasonic waves by negative refraction in phononic crystals," AIP Advances, vol. 6, pp. 121606, 2016

[50] R. Lanz and P. Muralt, "Bandpass filters for 8 GHz using solidly mounted bulk acoustic wave resonators," in IEEE Transactions on Ultrasonics, Ferroelectrics, and Frequency Control, vol. 52, no. 6, pp. 938-948, June 2005

[51] T F Krauss "Slow light in photonic crystal waveguides," J. Phys. D: Appl. Phys., vol. 40, pp. 2666–2670, 2007

[52] V. Laude, J. Beugnot, S. Benchabane, Y. Pennec, B. Djafari-Rouhani, N. Papanikolaou, J. Escalante, and A. Martinez, "Simultaneous guidance of slow photons and slow acoustic phonons in silicon phoxonic crystal slabs," Opt. Express 19, 9690-9698 (2011)

[53] Chen. L S, Kuo. C H, Ye. Z "Acoustic imaging and collimating by slabs of sonic crystals made from arrays of rigid cylinders in air," Appl. Phys. Lett., vol. 85, pp. 1072-1074, 2004

[54] Shi. Jinjie, Lin. Sz-Chin Steven, Huang. Tony Jun "Wide-band acoustic collimating by phononic crystal composites," Applied Physics Letters, vol. 92, pp. 111901, 2008

[55] Wang Y., Wang Y., Wu B., Chen W. and Wang, Y. (February 26, 2020). "Tunable and Active Phononic Crystals and Metamaterials." ASME. Appl. Mech. Rev. July 2020; 72(4): 040801

[56] R H Olsson III and I El-Kady "Microfabricated phononic crystal devices and applications," Meas. Sci. Technol., vol. 20, pp. 012002, 2009

[57] Hopkins, P.E., Phinney, L.M., Rakich, P.T. et al. Phonon considerations in the reduction of thermal conductivity in phononic crystals. Appl. Phys. A 103, 575–579 (2011)

[58] Yu, J., Mitrovic, S., Tham, D. et al. Reduction of thermal conductivity in phononic nanomesh structures. Nature Nanotech 5, 718–721 (2010)

[59] Yang Ronggui and Chen Gang "Thermal conductivity modeling of periodic two-dimensional nanocomposites," Phys. Rev. B, vol. 69, pp. 195316, 2004

[60] Yasser Adou, "Acoustic Properties of the South Pole Ice for Astrophysical Neutrino Detection," Ph.D. dissertation, Dept. Physics and Astronomy, Ghent University, Belgium, 2012

[61] Khelif Abdelkrim, Adibi Ali, *Phononic Crystals Fundamentals and Applications*, 2016

[62] Martin Maldovan, Edwin L. Thomas, *Periodic Materials and Interference Lithography: for Photonics, Phononics and Mechanics*, 2009

[63] W. Wang and D. Weinstein, "Acoustic Bragg reflectors for Q-enhancement of unreleased MEMS resonators," 2011 Joint Conference of the IEEE International Frequency Control and the European Frequency and Time Forum (FCS) Proceedings, San Francisco, CA, USA, 2011, pp. 1-6

[64] Jing Wang, Z. Ren and C. T. -. Nguyen, "1.156-GHz self-aligned vibrating micromechanical disk resonator," in IEEE Transactions on Ultrasonics, Ferroelectrics, and Frequency Control, vol. 51, no. 12, pp. 1607-1628, Dec. 2004

[65] Mizutani, U.; Sato, H. The Physics of the Hume-Rothery Electron Concentration Rule. Crystals 2017, 7, 9

[66] Lingyun Yao, Guoqi Jiang, Fei Wu, Jinyu Luo, "Band structure computation of two-dimensional and three-dimensional phononic crystals using a finite element-least square point interpolation method," Applied Mathematical Modelling, vol. 76, pp. 591-606, 2019

[67] Lucklum, F.; Vellekoop, M.J. Design and Fabrication Challenges for Millimeter-Scale Three-Dimensional Phononic Crystals. Crystals 2017, 7, 348

[68] Humberto Campanella Pineda, *Thin-film Bulk Acoustic Wave Resonators (FBAR): Fabrication, Heterogeneous Integration with CMOS Technologies and Sensor Applications*, 2008

[69] Ching-Liang Wei, Ying-Chung Chen, Chien-Chuan Cheng, Kuo-Sheng Kao, Da-Long Cheng, Chung-Jen Chung, "Highly Sensitive UV Sensors Based on SMR Oscillators," Procedia Engineering, vol. 36, pp. 468-475, 2012

[70] G. Piazza, P. J. Stephanou and A. P. Pisano, "Piezoelectric Aluminum Nitride Vibrating Contour-Mode MEMS Resonators," in Journal of Microelectromechanical Systems, vol. 15, no. 6, pp. 1406-1418, Dec. 2006

[71] Abdolvand, R.; Bahreyni, B.; Lee, J.E.-Y.; Nabki, F. Micromachined Resonators: A Review. Micromachines 2016, 7, 160

[72] Kun Wang, Ark-Chew Wong and C. T. -. Nguyen, "VHF free-free beam high-Q micromechanical resonators," in Journal of Microelectromechanical Systems, vol. 9, no. 3, pp. 347-360, Sept. 2000

[73] A. Zaman, A. Alsolami, I. F. Rivera and J. Wang, "Thin-Piezo on Single-Crystal Silicon Reactive Etched RF MEMS Resonators," in IEEE Access, vol. 8, pp. 139266-139273, 2020

[74] C.S. Li, M.H. Li, C.C. Chen, C.H. Chin and S.S. Li, "A Low-Voltage CMOS-Microelectromechanical Systems Thermal-Piezoresistive Resonator with Q>10000," IEEE Electron Device Letters, vol. 36, no. 2, pp. 192-194, Feb. 2015

[75] M.K. Zalalutdinov, J.D. Cross, J.W. Baldwin, B.R. Ilic, W. Zhou, B.H. Houston and M. Jeevak, "CMOS-Integrated RF MEMS Resonators," Journal of Microelectromechanical Systems, vol. 19, no. 4, pp. 807-815, Aug. 2010
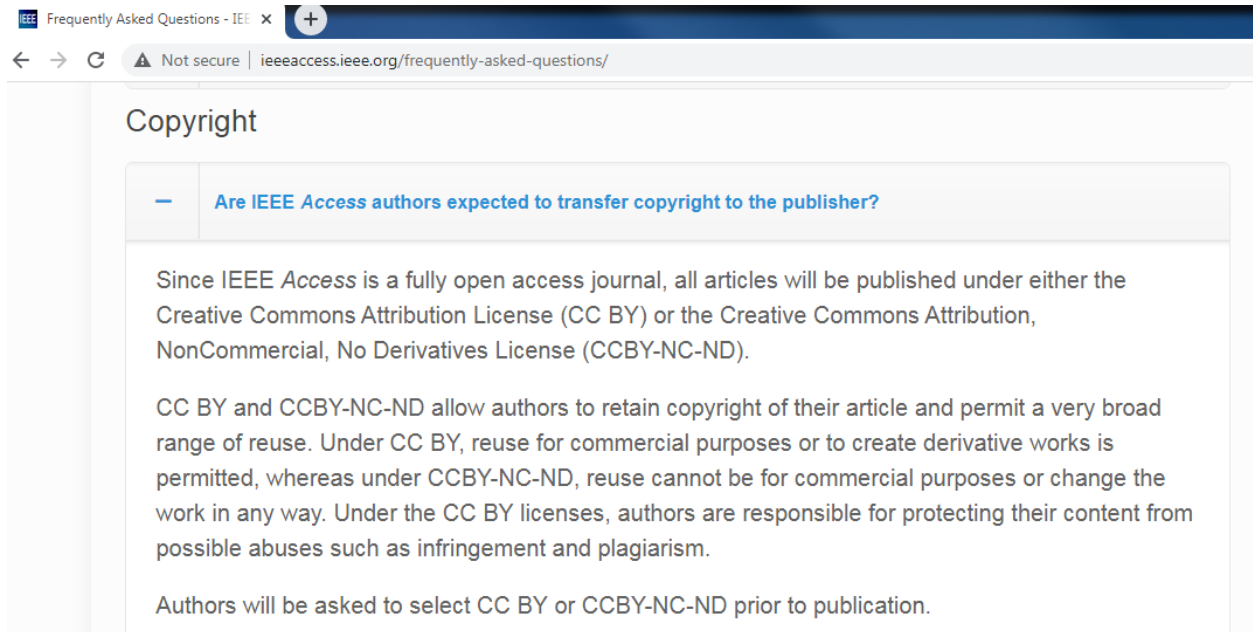
[76] J. Wang and C.T.C. Nguyen, "1.156-GHz self-aligned vibrating micromechanical disk resonator," IEEE Transactions on Ultrasonics, Ferroelectrics, and Frequency Control, vol. 51, no. 12, pp. 1607-1628, Dec. 2004

[77] U. Zaghloul and G. Piazza, "Highly Scalable NEMS Relays With Stress-Tuned Switching Voltage Using Piezoelectric Buckling Actuators," IEEE Transactions on Electron Devices, vol. 61, no. 10, pp. 3520-3528, Oct. 2014

[78] M.H. Li, W.C. Chen and S.S. Li, "Realizing Deep-Submicron Gap Spacing for CMOS-MEMS Resonators," IEEE Sensors Journal, vol. 12, no. 12, pp. 3399-3407, Dec. 2012

[79] J.R. Clark, W.T. Hsu, M.A. Abdelmoneum and C. T. C. Nguyen, "High-Q UHF micromechanical radial-contour mode disk resonators," Journal of Microelectromechanical Systems, vol. 14, no. 6, pp. 1298-1310, Dec. 2005

[80] L.W. Hung, C.T.C. Nguyen, Y. Xie, Y.W. Lin, S.S. Li and Z. Ren, "UHF Micromechanical Compound-(2,4) Mode Ring Resonators With Solid-Gap Transducers," 2007 IEEE International Frequency Control Symposium, Geneva, 2007, pp. 1370-1375

[81] C.-M. Lin, W.-C. Lien, V.V. Felmetsger, M.A. Hopcroft, D.G. Senesky, A.P. Pisano, "AlN thin films grown on epitaxial 3C–SiC (100) for piezoelectric resonant devices," Appl. Phys, Lett. 97(14), 141907 (2010)

[82] H. Chandrahalim, S. A. Bhave, R. Polcawich, J. Pulskamp, D. Judy, R. Kaul and M. Dubey, "Performance comparison of Pb(Zr0.52Ti0.48)O3-only and Pb(Zr0.52Ti0.48)O3-on-silicon resonators," Appl. Phys. Lett. 93 233504 (2008)

[83] R. Abdolvand, H.M. Lavasani, G.K. Ho and F. Ayazi, "Thin-film piezoelectric-on-silicon resonators for high-frequency reference oscillator applications," IEEE Transactions on Ultrasonics, Ferroelectrics, and Frequency Control, vol. 55, no. 12, pp. 2596-2606, December 2008

[84] B. P. Harrington, M. Shahmohammadi, and R. Abdolvand, "Toward ultimate performance in GHz MEMS resonators: Low impedance and high Q," Proc. IEEE Micro Electro Mechanical Systems Conf., Jan. 2010, pp. 707–710

[85] J. Mencik, E. Quandt, D. Munzm, "Elastic modulus of TbDyFe films—a comparison of nanoindentation and bending measurements," Thin Solid Films, Vol. 287, pp. 208-213, Oct. 1996

[86] K. Girija Sravani et al., "Design and Performance Analysis of Low Pull-In Voltage of Dimple Type Capacitive RF MEMS Shunt Switch for Ka-Band," IEEE Access, vol. 7, pp. 44471-44488, Apr. 2019

[87] V. K. Varadan, K. J. Vinoy , K. A. Jose , RF MEMS and Their Applications, England, 2002

[88] S. Pourkamali, G. K. Ho, F. Ayazi, "Low-Impedance VHF and UHF Capacitive Silicon Bulk Acoustic Wave Resonators—Part I: Concept and Fabrication," IEEE Transactions on Electron Devices, VOL. 54, NO. 8, AUGUST 2007

[89] Z. Hao, S. Pourkamali, F. Ayazi, "VHF Single-Crystal Silicon Elliptic Bulk-Mode Capacitive Disk Resonators—Part I: Design and Modeling," Journal of Microelectromechanical Systems, , VOL. 13, NO. 6, DECEMBER 2004

[90] D. M. Allen and I. A. Routledge, "Anisotropic etching of silicon. a model diffusion-controlled reaction," IEE Proceedings I - Solid-State and Electron Devices, vol. 130, no. 2, pp. 49-56, April 1983

[91] R. Abdolvand, F. Ayazi, "An advanced reactive ion etching process for very high aspect-ratio sub-micron wide trenches in silicon," Sens. Actuators, A Phys. 2008;144:109–116

[92] D. Xu, B. Xiong, G. Wu, Y. Ma, Y. Wang and E. Jing, "Characterization of wafer-level XeF2 Gas-phase Isotropic Etching For MEMS Processing," 2012 7th IEEE International Conference on Nano/Micro Engineered and Molecular Systems (NEMS), Kyoto, 2012, pp. 274-277

[93] D. Xu, B. Xiong, G. Wu, Y. Wang, X. Sun and Y. Wang, "Isotropic Silicon Etching With XeF2 Gas for Wafer-Level Micromachining Applications," in Journal of Microelectromechanical Systems, vol. 21, no. 6, pp. 1436-1444, Dec. 2012

[94] Q. Chen, J. Fang, H. Ji and K. Varahramyan, "Fabrication of SiO2 Microcantilever Using Isotropic Etching With ICP," IEEE Sensors Journal, vol. 7, no. 12, pp. 1632-1638, Dec. 2007

[95] Y. Shin, Y. Kim, S. Lee and J. Park, "Single-mask fabrication of micro-probe electrode array with various tip heights and sharpness using isotropic and anisotropic etching," Micro & Nano Letters, vol. 13, no. 9, pp. 1245-1247, 9 2018

[96] M. Chabloz, J. Jiao, Y. Yoshida, T. Matsuura and K. Tsutsumi, "A method to evade microloading effect in deep reactive ion etching for anodically bonded glass-silicon structures," Proceedings IEEE 13th Annual International Conference on Micro Electro Mechanical Systems (Cat. No.00CH36308), Miyazaki, Japan, 2000, pp. 283-287

[97] M. A. Gosalvez, Y. Zhou, Y. Zhang, G. Zhang, Y. Li and Y. Xing, "Simulation of microloading and ARDE in DRIE," 2015 Transducers - 2015 18th International Conference on Solid-State Sensors, Actuators and Microsystems (TRANSDUCERS), Anchorage, AK, 2015, pp. 1255-1258

[98] J. Karttunen, J. Kiihamaki, S. Franssila, "Loading effects in deep silicon etching," In Micromachining and Microfabrication Process Technology VI; SPIE: Bellingham, WA, 2000; Vol. 4174

[99] I. Rivera, A. Avila, J. Wang, "Fourth order contour mode ZnO-on-SOI disk resonators for mass sensing applications," Actuators, 4:60–76, 2015

[100] P. Muralt, J. Conde, A. Artieda, F. Martin, M. Cantoni, "Piezoelectric materials parameters for piezoelectric thin films in GHz applications," International Journal of Microwave and Wireless Technologies, vol. 1, no. 1, pp. 19-27, 2009

[101] M. Spindler, S. Herold, J. Acker, E. Brachmann, S. Oswald, S. Menzel, G. Rane, "Chemical etching of Tungsten thin films for high-temperature surface acoustic wave-based sensor devices," Thin Solid Films, vol. 612, pp. 322-326, 2016

[102] Spahn, Olga Blum; Rowen, Adam M.; Cich, Michael Joseph; Peake, Gregory Merwin; Arrington, Christian L.; Nash, Thomas J. et al. Microfabricated wire arrays for Z-pinch., report, October 1, 2008; United States

[103] Boruah, Palash Jyoti et al. "Synthesis and Characterization of Oxygen Vacancy Induced Narrow Bandgap Tungsten Oxide (WO3−x) Nanoparticles by Plasma Discharge in Liquid and Its Photocatalytic Activity." Plasma Chemistry and Plasma Processing 40 (2020): 1019 − 1036

[104] Shao, F., Wenge Chen, H. Zhang and B. Ding. "Microstructure Evolution of W-Cu Alloy Wire after Hot-Swaging *." Materials Sciences and Applications, vol. 3, pp. 157-162, (2012)

[105] Deepak Bhatia, Himanshu Sharma, R.S. Meena, V.R. Palkar, "A novel ZnO piezoelectric microcantilever energy scavenger: Fabrication and characterization," Sensing and Bio-Sensing Research, vol. 9, pp. 45-52, 2016

[106] Sinha Nipun, Wabiszewski Graham E., Mahameed Rashed, Felmetsger Valery V., Tanner Shawn M., Carpick Robert W., Piazza Gianluca "Piezoelectric aluminum nitride nanoelectromechanical actuators," Applied Physics Letters, vol. 95, pp. 053106, 2009

[107] Mao Liu, Jiawei Xiang, Yongteng Zhong, "The band gap and transmission characteristics investigation of local resonant quaternary phononic crystals with periodic coating," Applied Acoustics, vol. 100, pp. 10-17, 2015

[108] Jie Zou, "High Quality Factor Lamb Wave Resonators," M.S. Thesis, Dept. E.E.C.S., University of California, Berkeley, 2012

[109] X. Wu, F. Bao, X. Zhou, Q. Wu, J. Liu and J. Bao, "Spider Web-Shaped Phononic Crystals for Quality Factor Improvement of Piezoelectric-on-Silicon MEMS resonators," 2019 IEEE International Ultrasonics Symposium (IUS), Glasgow, United Kingdom, 2019, pp. 1724-1726

[110] M. A. Khan, J. -F. Bao, L. R. Zafar, F. -H. Bao and Xin-Zhou, "Quality Enhancement of Centered Hole Thin Film Disc Resonator by Drilled Phononic crystals," 2019 IEEE Asia-Pacific Microwave Conference (APMC), Singapore, Singapore, 2019, pp. 977-979

Appendix A: Copyright Permissions

The permission below is for the use of the material in Chapter 3.

About the Author

Abdulrahman Alsolami received his B.S. in Electrical Engineering from King Abdulaziz University, Jeddah, Saudi Arabia in 2010 and the M.S. and PhD in Electrical Engineering in 2015 and 2020, respectively. He currently works as assistant professor in King Abdulaziz City for Science and Technology (KACST), Riyadh, Saudi Arabia. His main research is in RF circuits particularry in RF MEMS devices. His interest includes Modeling, Designing and Fabricating Micromachine devices for RF applications.